IJMMM International Journal of Minerals, Metallurgy and Materials 矿物冶金与材料学报（英文版）

Research progress on selective laser melting processing for nickel-based superalloy

Maohang Zhang, Baicheng Zhang, Yaojie Wen, and Xuanhui Qu

Cite this article as:
Maohang Zhang, Baicheng Zhang, Yaojie Wen, and Xuanhui Qu, Research progress on selective laser melting processing for nickel-based superalloy, *Int. J. Miner. Metall. Mater.*, 29(2022), No. 3, pp. 369-388. https://doi.org/10.1007/s12613-021-2331-1

View the article online at SpringerLink or IJMMM Webpage.

International Journal of Minerals, Metallurgy and Materials
Volume 29, Number 3, March 2022, Page 369
https://doi.org/10.1007/s12613-021-2331-1

Invited Review

Research progress on selective laser melting processing for nickel-based superalloy

Maohang Zhang[1)], *Baicheng Zhang*[1,2),✉], *Yaojie Wen*[1)], *and Xuanhui Qu*[1,2),✉]

1) Beijing Advanced Innovation Center Materials Genome Engineering, Institute for Advanced Materials and Technology, University of Science and Technology Beijing, Beijing 100083, China
2) Beijing Laboratory of Metallic Materials and Processing for Modern Transportation, Beijing 100083, China
(Received: 12 January 2021; revised: 12 July 2021; accepted: 17 July 2021)

Abstract: Selective laser melting (SLM), an additive manufacturing process mostly applied in the metal material field, can fabricate complex-shaped metal objects with high precision. Nickel-based superalloy exhibits excellent mechanical properties at elevated temperatures and plays an important role in the aviation industry. This paper emphasizes the research of SLM processed Inconel 718, Inconel 625, CM247LC, and Hastelloy X, which are typical alloys with different strengthening mechanisms and operating temperatures. The strengthening mechanism and phase change evolution of different nickel-based superalloys under laser irradiation are discussed. The influence of laser parameters and the heat-treatment process on mechanical properties of SLM nickel-based superalloys are systematically introduced. Moreover, the attractive industrial applications of SLM nickel-based superalloy and printed components are presented. Finally, the prospects for nickel-based superalloy materials for SLM technology are presented.

Keywords: selective laser melting; nickel-based superalloy; mechanical property

1. Introduction

Nickel-based superalloys have been popular in the industry owing to their extraordinary properties, such as excellent refractoriness and exceptional resistance to corrosion at low and high temperatures [1–2]. Gas turbines used in space aircraft and rocket engines are generally made from nickel-based superalloys [2]. According to one report [3], there are nearly 1.8 tons of nickel-based superalloys in a typical jet engine. These materials greatly contribute to the increased continuous operating life of jet engines to above 20000 h. Hot components of aeroengines such as compressors, turbines, and combustion chambers are mainly composed of nickel-based superalloys as shown in Fig. 1, and their corresponding service temperatures are listed. The entrance to the turbine, in particular, almost completely uses specific types of nickel-based superalloys that can maintain high strength and stability at ultrahigh temperatures in order to increase turbine entry temperature (TET) and improve engine performance [4–5]. For instance, Inconel® superalloy has been selected for the port of entry of the F119-PW-100 (an afterburning turbofan engine for F-22 Raptor advanced tactical fighters), for which the TET can approach 1600–2200°C.

In order to reduce segregation or thermal cracking when casting in a large size, powder metallurgy (PM) has been developed to avoid the aforementioned problems and aims to reach the level of forging, which typically processes a sequence of master alloy melting, atomization, hot compaction, hot extrusion, isothermal forging, and heat treatment [6–7]. Nevertheless, prior particle boundary and thermally-induced pores impose restrictions on PM superalloy. High cost and low flexibility during formation and densification also depress the economic efficiency and commercial potential of PM technic [8].

Additive manufacturing (AM), also known as 3D printing or rapid prototyping, refers to a process wherein objects are made by joining materials layer upon layer according to 3D model data, which is distinguished from traditional subtractive manufacturing methods by omittance of cutters and molds, simplification of production process, and reduction of cost [9]. Among a dozen categories of AM process, powder bed fusion (PBF) and direct energy deposition are two main techniques applied in metal component manufacturing [10]. Selective laser melting (SLM), which belongs to PBF, shows high potential for near-net-shape fabrication with complex geometries, which cannot be readily prepared by the other traditional manufacturing techniques [11]. Application of SLM processing metals such as titanium alloy [12], steel [11], and nickel has been booming recently. Fig. 2 illustrates the SLM fabrication system and main process parameters [13–14]. Metallic powder is melted and fused by a high-energy laser beam controlled by two sets of vibrating mirror

✉ Corresponding authors: Baicheng Zhang E-mail: zhangbc@ustb.edu.cn; Xuanhui Qu E-mail: quxh@ustb.edu.cn

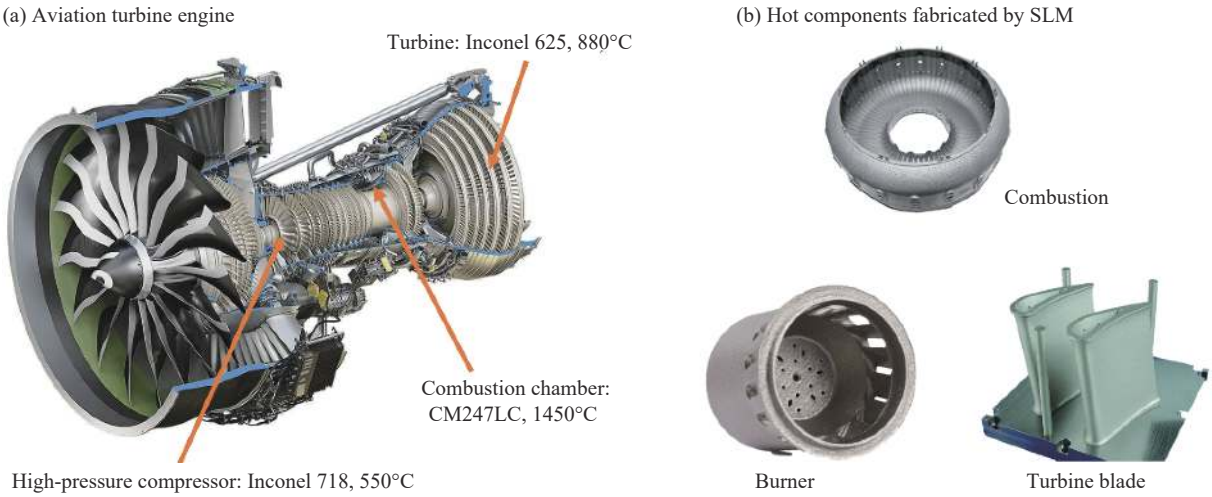

Fig. 1. (a) Application of nickel-based superalloys in the modern aviation turbine engine and service temperature; (b) examples of mature commercial hot component products fabricated by selective laser melting (SLM).

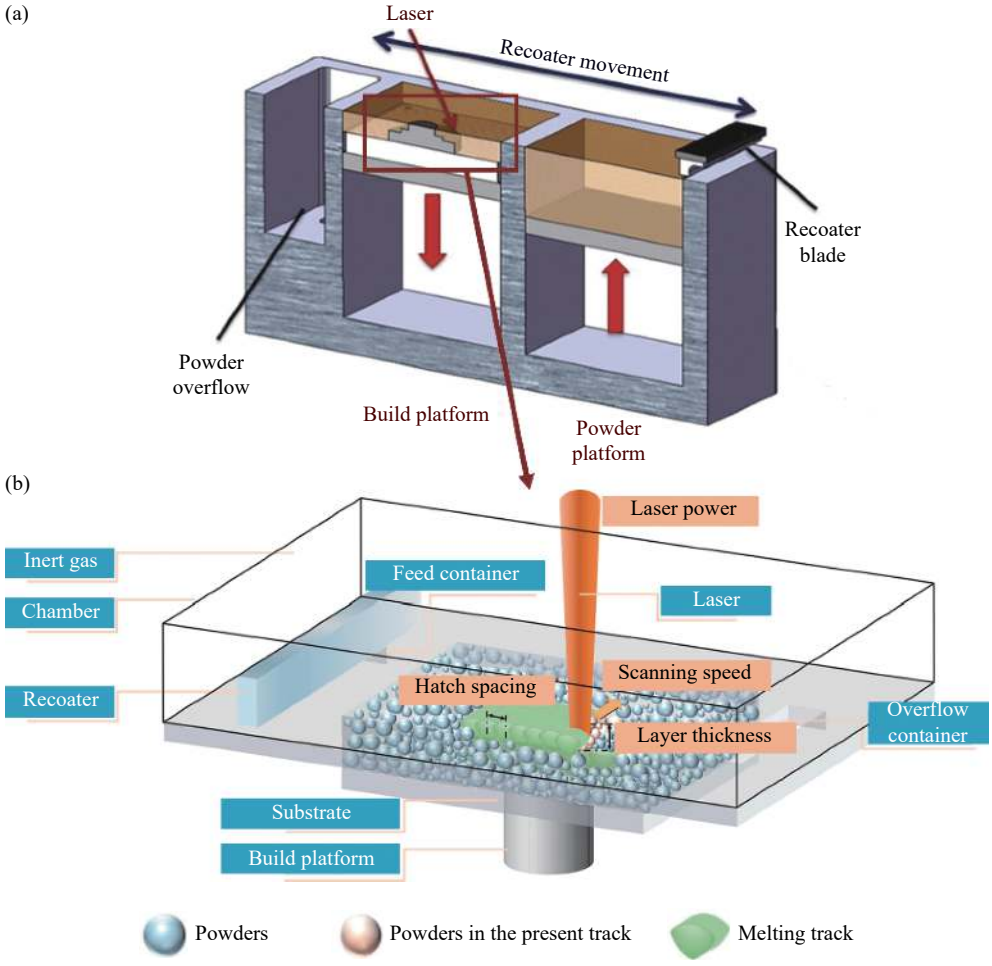

Fig. 2. Illustration of (a) SLM fabrication system [13] and (b) main process parameters [14]. Metallic powder is laid from the powder platform to the build platform as blade movement and then melted by laser to finish one layer. This process is repeated until the complete component is finished. Main process parameters include laser power, scanning speed, hatch spacing, layer thickness, and scanning strategy. (b) is reprinted from *Prog. Mater. Sci.*, 104, W.H. Yu, S.L. Sing, C.K. Chua, C.N. Kuo, and X.L. Tian, Particle-reinforced metal matrix nanocomposites fabricated by selective laser melting: A state of the art review, 330-379, Copyright 2019, with permission from Elsevier.

systems, thus achieving a rated two-dimension pattern. In this way, the printed component is produced layer by layer and is highly influenced by powder quality (chemical composition, size distribution, sphericity, and flowability) and process parameters (laser power, scanning speed, hatch space, layer thickness, and scanning strategy) [15–16].

It should be noted that the microstructure of nickel-based superalloy fabricated by SLM is quite different from that of

traditional techniques due to complicated thermal history and *in-situ* phase transition during cyclically rapid melting and solidification. This leads to different manufacturing deficiencies and mechanical properties [17]. Predominate-oriented columnar crystal along the building direction with a small region of equiaxed crystal leads to strong anisotropy. Fine grains with diameters below 10 μm, which is almost a quarter of the cast, generate remarkable mechanical properties. Porosity and cracks induced during the SLM process cause inevitable deterioration. Therefore, the main task of optimizing SLM parameters is avoiding harmful phases, reducing porosity and crack, and simultaneously acquiring the γ′ phase. Commonly, a solution treatment at high temperature is carried out to completely dissolve the precipitation phase; an aging treatment follows to precipitate a uniform and fine-strengthened phase (γ′ or γ″ phase) during the actual production process [18].

In order to extend our research vision, four specific representative alloys were chosen to display the progress of SLM nickel-based superalloy in the following sections. Despite their different strengthening mechanisms, common issues and respective challenges are discussed.

2. SLM precipitation strengthening nickel-based superalloy

Large amounts of γ′ phase promote the mechanical properties of SLM nickel-based superalloy such as Inconel 738, Inconel 939, K418, K536, K4202, Rene41, and CM247LC [19–24]. Within Inconel 718, the γ″ phase plays a dominant role due to high niobium content. γ′ phase can possess a stable microstructure at elevated temperatures, keeping coherent or semi-coherent with the matrix phase. However, the metastability of the γ″ phase makes it transform into a stable orthorhombic δ-Ni_3Nb phase during long-term exposure at temperatures of >650°C [25]. Therefore, CM247LC and Inconel 718 were chosen for the following discussion.

2.1. Research progress of SLM CM247LC alloy (ultrahigh service temperature)

CM247LC is a typical precipitation-strengthening superalloy, which is obtained by optimizing the composition of directionally solidified (DS) superalloys "Mar M247." The chemical composition of CM247LC is listed in Table 1 [26]. It has excellent resistance to grain boundary cracking during DS casting and high-temperature creep [27]. However, high aluminum content impairs weldability, although it contributes to the formation of the high volume of γ′ phase. Strategies including the optimization of SLM parameters, application of hot isostatic pressing (HIP), and tuning of the chemical composition have been widely studied to reduce crack density.

Table 1. Chemical composition of CM247LC [26] wt%

C	Cr	Ni	Co	Mo	W	Ta	Ti	Al	B	Zr	Hf
0.07	8	Bal.	9	0.5	10	3.2	0.7	5.6	0.015	0.01	1.4

2.1.1. Laser parameter optimization and crack reduction

Under high service temperature and high-stress loading, the SLM superalloy component is sensitive to crack generation. The major aims of laser parameters optimization are to avoid cracking and increase density.

There are four main cracking sources for superalloy: (1) solidification cracking (caused by tensile stresses in liquid–solid two phases region and a high fraction of solid precipitation), (2) grain boundary liquation cracking (caused by local dissolution of grain boundary phases), (3) strain aging cracking (SAC, intergranular cracks in the heat affected zone area region, a microcrack initiation caused by a lattice mismatch between carbide and matrix that occurs during heat treatment or during high-temperature application), and (4) ductility dip cracking (DDC, due to the grain boundary sliding and high-temperature creep) [28]. Solidification cracks and grain boundary cracks occur at the same time during the SLM process for CM247LC. The likely mechanism for solidification cracks is the unique dendrite morphology microstructure. SAC and DDC are considered as the most feasible explanations for grain boundary cracks, while no direct evidence has proved liquefying cracking is the prime cause [27].

A large amount of aluminum is added into CM247LC to increase the amount of γ′ phase, rendering it prone to cracking during the SLM process, thus sacrificing weldability compared with Inconel 718, Inconel 625, and Hastelloy X, as shown in Fig. 3(a). Some low melting point phase and inconsonant solidification rates result in micro-cracks and residual stress tears in the follow-up forming process, thereby introducing the initiation and propagation of cracks.

Cracks and pores distributed in SLM components under undesirable laser parameters are also shown in Fig. 3(b)–(c). Microcrack reduction and proper heat treatment processes have been widely studied. Cater *et al.* [27] investigated the influence of laser parameters on cracks in the SLM part. Under higher energy density, the effect mainly appears as solidification cracks in the inter-dendritic region, while under lower energy density, cracks are mainly caused by the carbides distributed in the grain boundary. Under a certain energy density, crack density increases with increasing scanning speed and decreasing hatch distance. The effect of the "island" scanning strategy on internal cracks has also been studied; it was found that it tended to occur DDC with high grain boundary angles [16].

Catchpole-Smith *et al.* [29] compared the effects of fractal scan strategies (Hilbert and Peano-Gosper curve) and island scan strategy on internal cracks. Defects and cracks show more obvious directivity under the island scan strategy, while fractal scan strategies significantly reduce void defects and shorten cracks (although they tend to be slightly wider). Traditional "island" strategy (5 mm × 5 mm discrete scanning region, 25 μm thickness, 100 W laser power, and 400 $mm \cdot s^{-1}$ scanning speed) produces only 96.0% density, which is clearly lower than those of new strategies (up to 98.0%) as shown in Fig. 4(a). According to neutron tomography in Fig.

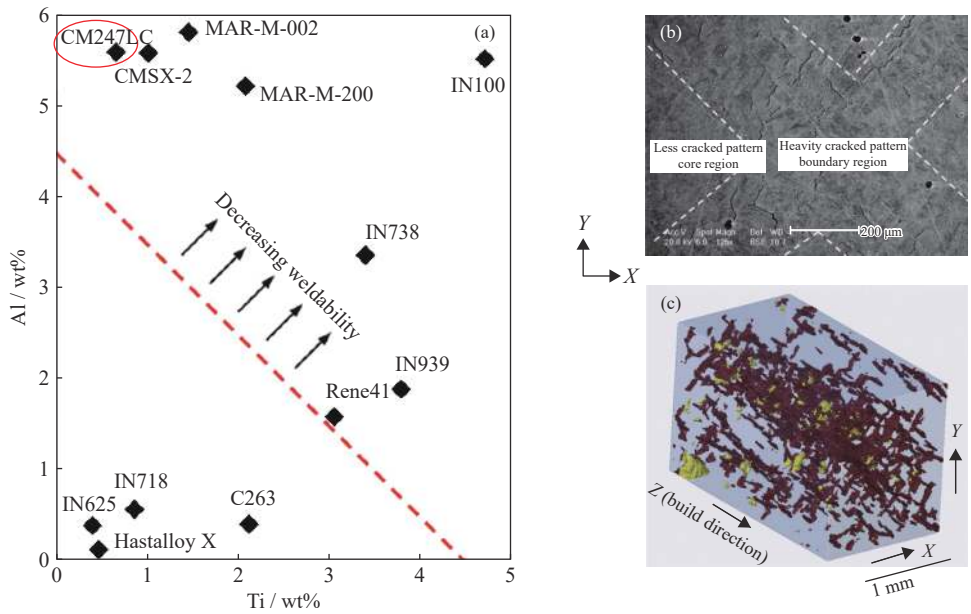

Fig. 3. (a) Weldability evolution of nickel-based superalloy with Ti and Al content: weldability deteriorates with increasing Ti and Al content and is considered poor above the red dash line [29]. (b) Scanning electron microscope (SEM) image of cracks and pores in SLM CM247LC component; (c) Micro-computerized tomography (CT) data (the red part represents cracks and the yellow represents pores) [16].

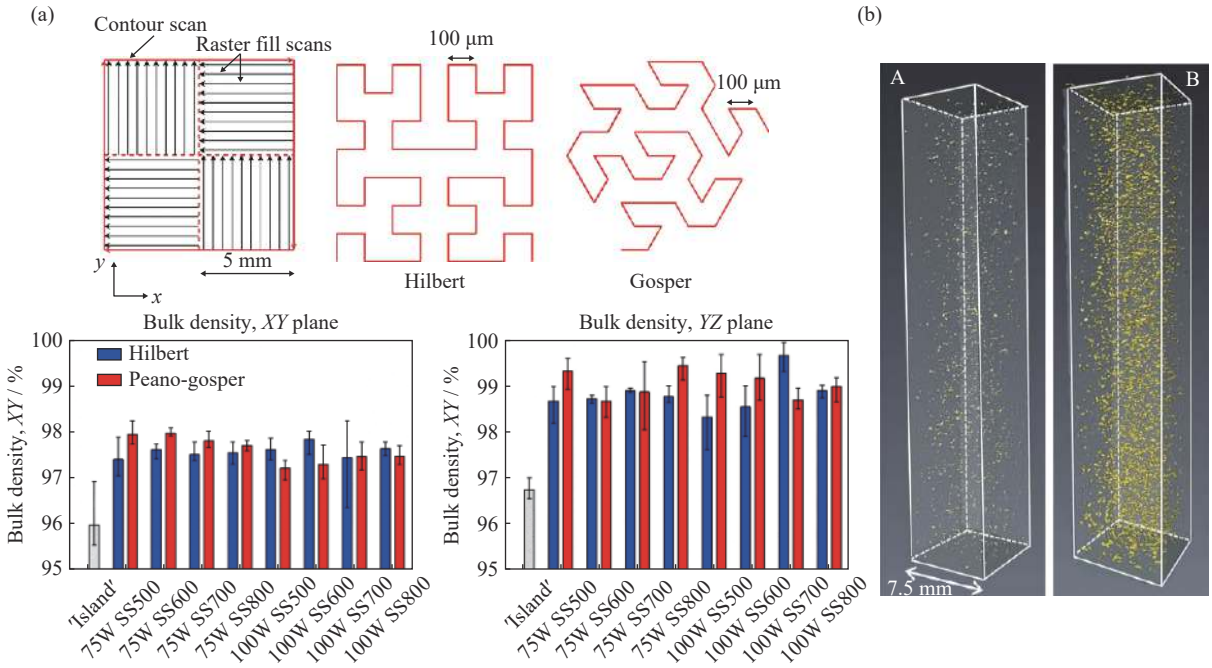

Fig. 4. (a) Schematic of different strategies and corresponding densities under different parameters observed from two perpendicular sections. 'Gosper' and 'Hilbert' strategies significantly increase density compared to 'island' [29]. (b) Neutron tomography images of different parts from the same components, pores with diameters from 15 μm to 40 μm distribute within the body. (b) is reprinted from *Mater. Lett.*, 230, R.P. Turner, C. Panwisawas, Y. Lu, I. Dhiman, H.C. Basoalto, and J.W. Brooks, Neutron tomography methods applied to a nickel-based superalloy additive manufacture build, 109-112, Copyright 2018, with permission from Elsevier.

4(b), the particle diameter of most pores ranges from 15 to 40 μm [30], indicating they come from un-melted particles. However, pores in the nanoscale are not detected by neutron tomography, making it difficult to get an absolutely accurate density value.

Scholars have studied other methods of reducing residual stress. Kalentics *et al.* [31] combined laser shock peening technology to convert the tension residual stress into compressive residual stress in the SLM parts, thus decreasing crack density. A 95% reduction was achieved compared to the only-SLM part. Bidron *et al.* [32] used laser cladding to repair CM247LC components. They investigated the influence of different preheating temperatures on cracks. When preheating temperature exceeded 1100°C, the crack density

decreased due to a decrease in the γ′ phase contents.

2.1.2. Microstructure of as-printed and heat-treatment CM247LC

The microstructure of CM247LC fabricated by SLM is mainly composed of columnar crystals in which most elongated and a few equiaxed sub-crystals distribute, and strong cube texture can be observed along the build direction. The diameter of the sub-crystal is just several micrometers. γ′ precipitates distributed within the cell are about 5–10 nm, while those distributing at grain and cell boundaries are about 50 nm. γ/γ′ eutectic with some small particles around 50 nm exists in the sub-grain boundary. High densities of γ′ precipitates, hafnium/tantalum/tungsten/titanium-rich precipitates and dislocation are both found distributed throughout adjacent cells and grains due to complex heating/cooling cycles as shown by transmission electron microscope (TEM) image and X-ray mapping in Fig. 5 [33].

After heat treatment, dislocation densities between cells decrease due to recovery, γ′ precipitates coarsen due to recrystallization, and much finer, randomly-oriented grains are formed, which are indicated by backscattered electrons (BSE) SEM images in Fig. 6 [34–35]. By compositional analysis, particles formed after heat treatment are mainly MC carbides rich in titanium, hafnium, tantalum, molybdenum, tungsten, and a small amount of spherical oxides rich in hafnium and aluminum. In the composition mapping, titanium, hafnium, and chromium aluminum tend to segregate at grain boundaries, while nickel and cobalt are higher within

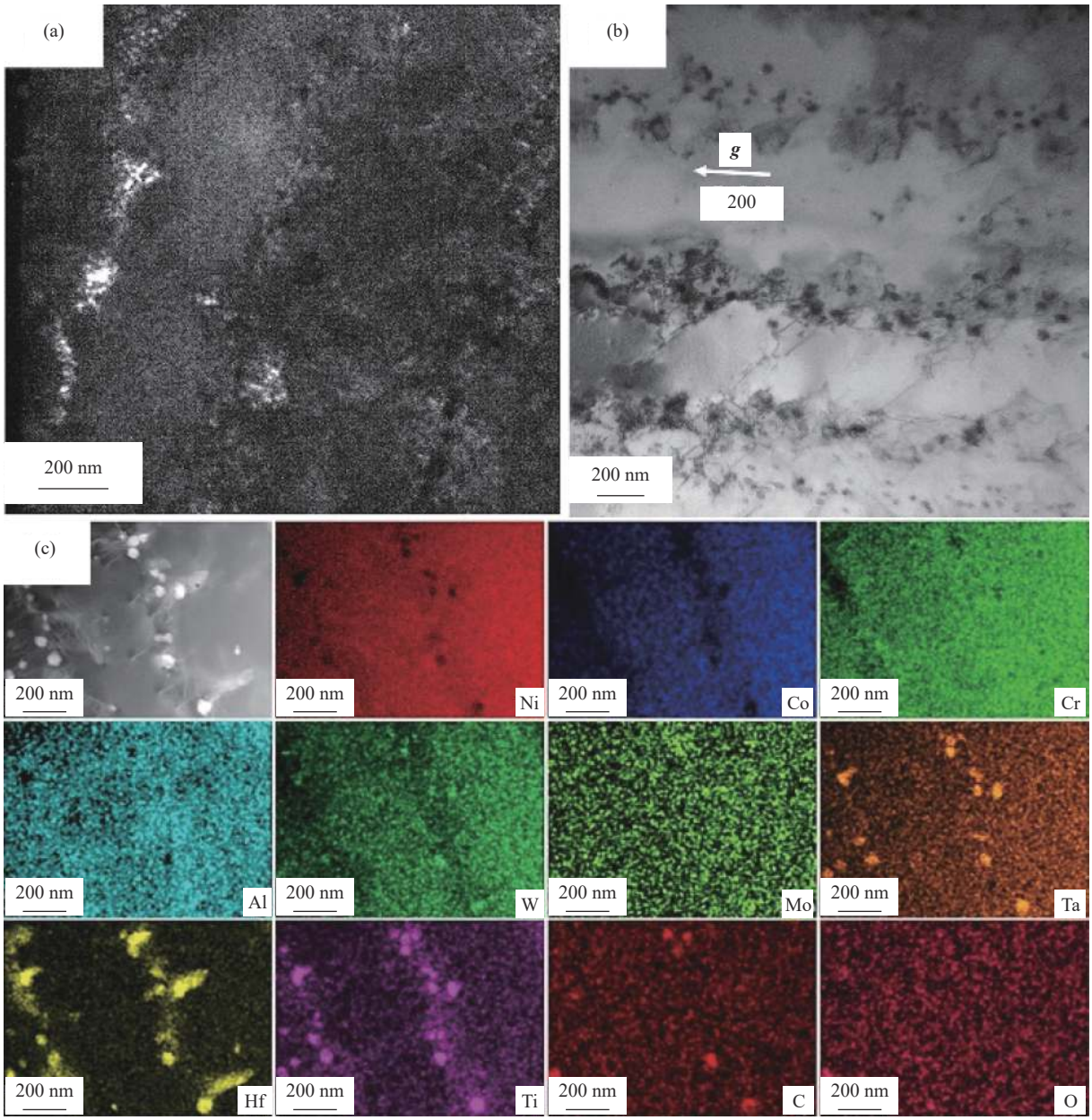

Fig. 5. (a) TEM dark field image of high content γ′ phase reflections; (b) TEM bright field image of dislocation density (using operating vector *g* = 200); (c) X-ray mapping of Hf/Ta/W/Ti-rich precipitates. Reprinted from *Acta Mater.*, 128, X.Q. Wang, L.N. Carter, B. Pang, M.M. Attallah, and M.H. Loretto, Microstructure and yield strength of SLM-fabricated CM247LC Ni-superalloy, 87-95, Copyright 2017, with permission from Elsevier.

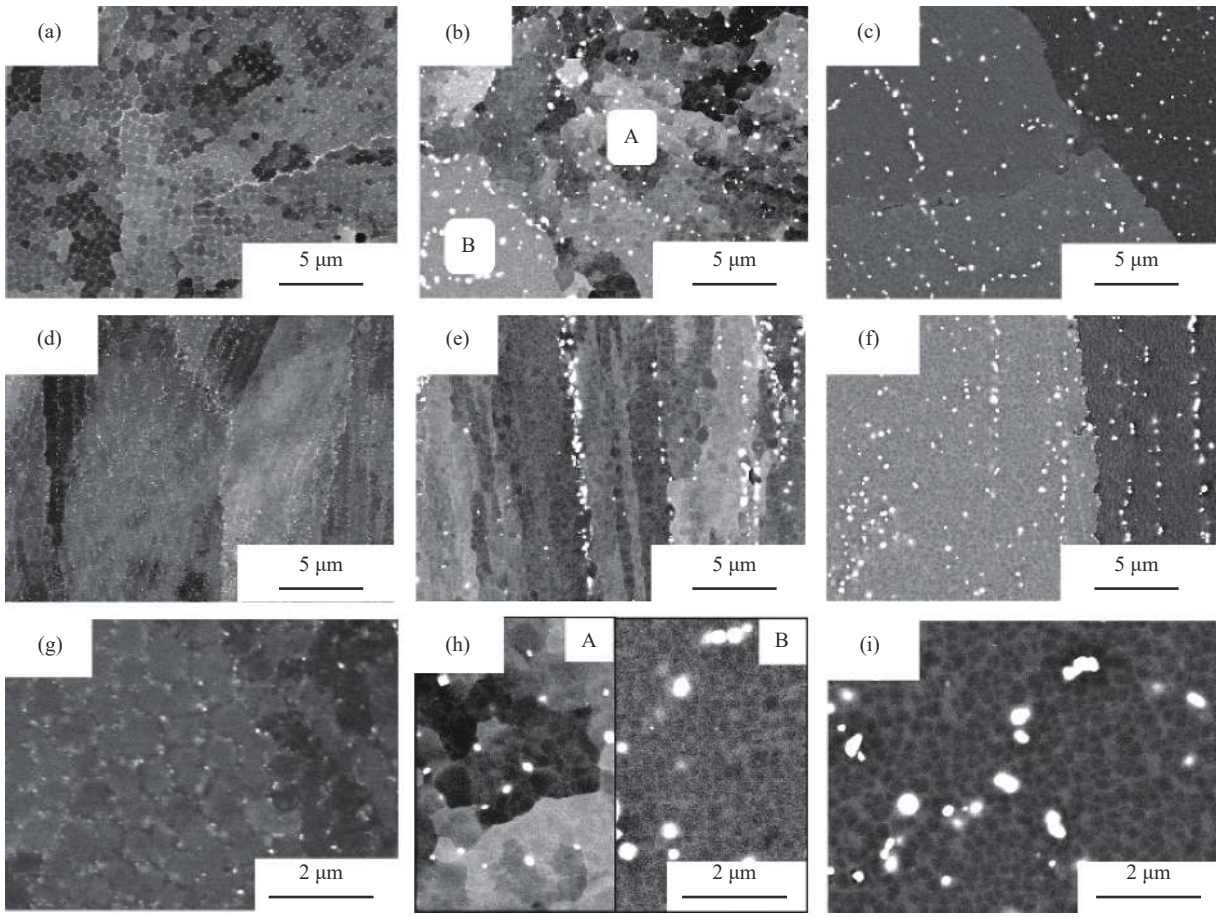

Fig. 6. BSE SEM images of transverse sections at high magnifications of (a) as-SLM, (b) SLM + heat treatment (HT) (1230°C) and (c) SLM + HT (1240°C) CM247LC. Longitudinal sections of the material in the three representative microstructural states are shown in (d–f) and cellular/grain morphology and γ′ phase are shown in (g–i). Note that in (b) and (h), A is a non-recrystallized region and B is a recrystallized region. Reprinted from *Mater. Sci. Eng. A*, 674, R. Muñoz-Moreno, V.D. Divya, S.L. Driver, O.M.D.M. Messé, T. Illston, S. Baker, M.A. Carpenter, and H.J. Stone, Effect of heat treatment on the microstructure, texture and elastic anisotropy of the nickel-based superalloy CM247LC processed by selective laser melting, 529-539, Copyright 2016, with permission from Elsevier.

grains [33–35]. The elemental distribution also affects the crack appearance where a higher content of hafnium and aluminum are detected [30,33].

DSC (differential scanning calorimetry) and CAPLHAD are used to analyze the phase transform temperature [34–36]. As temperature increases, two exothermic reactions occur at 450°C and 740°C, mainly due to the growth of fine intercellular γ′ phase and grain boundary γ′ phase films and transformation of MC carbides into M_6C and $M_{23}C_6$. At approximately 1254°C, γ′ phase precipitates begin to dissolve until approximately 1265°C. The solidus temperature is 1279°C, and the carbide begins to dissolve from 1357 to 1373°C, which is the liquidus temperature. Thermo-Calc has predicted a slightly different temperature. Boswell *et al.* [36] investigated the microstructure evolution during the heating process. They found that cracks are intensified with the collective influence of the γ′ phase, ductility reduction, and residual stress during the reheating process. When the preheating temperature is below 700°C, it is possible for DDC to occur. As the temperature increases to 750°C, SAC tends to occur. When the temperature reaches over 950°C, the presence of oxygen affects crack formation.

2.1.3. Mechanical property of as-printed and post-treatment CM247LC

Although the SLM CM247LC sample contains a high volume of γ′ precipitates, the mechanical property cannot be satisfactory as expected due to cracks produced during heating/cooling cycles [26]. Few reports have recorded a strength test for SLM CM247LC. Muñoz-Moreno *et al.* [35] found Young's modulus of SLM CM247LC to have strong anisotropy factors along the *Z* and *Y* directions, which is up to 233 GPa. Different heat treatments can reduce anisotropy by eliminating dense texture. Wang *et al.* [33] performed tensile tests on SLM CM247LC components and compared them with other processes, as shown in Fig. 7(a). Both ultimate tensile strength (UTS) and yield strength (YS) are better than those of the cast CM247LC after standard heat treatment, which results from high dislocation density, Hf/W/Ti/Ta-rich precipitates, and γ′ precipitates. However, the ductility of SLM components is extremely poor, and fracturing outside the gauge length even occurs. Heat treatment and HIP increase ductility to a certain extent but cannot make up completely. Micro-CT results (Fig. 7(b)) show that HIP can close internal cracks, but surface-connected cracks remain. Indeed,

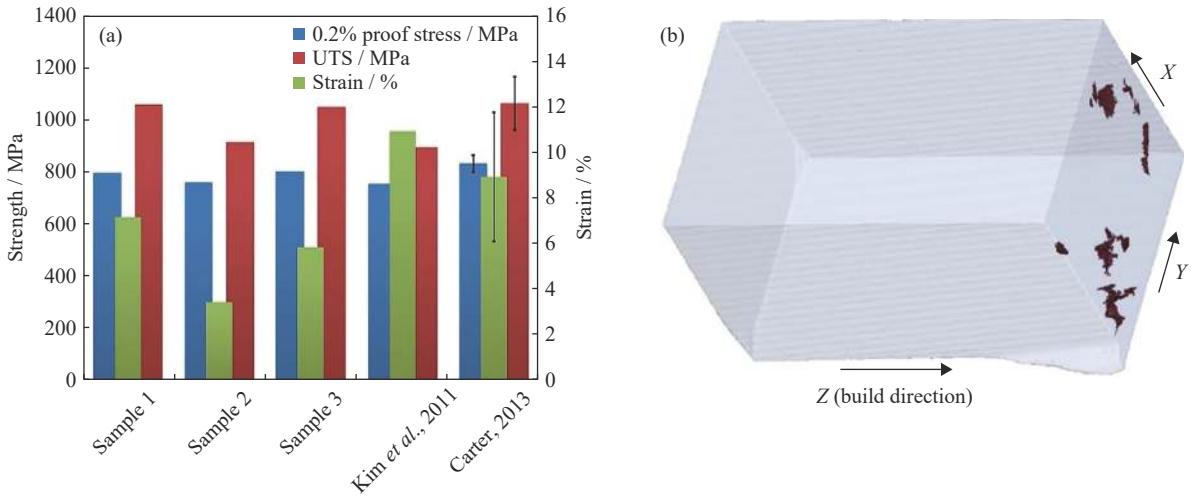

Fig. 7. (a) Strength and stain of SLM CM247LC samples (samples 1–3 are as-printed, Kim's is cast + HT and Carter's is SLM + HIP. The strength of as-printed sample is quite good with cast + HT; HIP can promote strain but make no improvement in strength. (b) Micro-CT data of SLM CM247LC after HIP where the red part represents cracks and pores [16]. (a) is reprinted from *Acta Mater.*, 128, X.Q. Wang, L.N. Carter, B. Pang, M.M. Attallah, and M.H. Loretto, Microstructure and yield strength of SLM-fabricated CM247LC Ni-superalloy, 87-95, Copyright 2017, with permission from Elsevier.

an adjustment in the chemical composition of CM247LC powder, such as reducing Al content, is fundamental to eliminating the influence of cracks and enhancing potential in AM.

2.2. Research progress of SLM Inconel 718 alloy (service temperature below 650°C)

Inconel 718, which is rich in niobium and mainly strengthened by γ″ phase, maintains stable mechanical properties up to 650°C and is widely employed in the aviation industry. Its chemical composition is listed in Table 2 [37]. In recent years, Inconel 718 has become the most favored metal material for SLM due to its outstanding weldability. Frontier exploration is not only performed in the laboratory but also ready for industrial production. Fig. 8 shows a specific monolithic thrust chamber made of Inconel 718 achieved by an SLM®280 selective laser melting machine, which is more efficient, stable, and lightweight. It minimizes individual process steps while combining multiple parts into a single component, thus reducing production time from months to days [38]. The goal of programming SLM Inconel 718 is to realize full density and to maintain or exceed forging levels, hence achieving more commercial applications.

Table 2. Chemical composition of EOS Inconel 718 powder [37] wt%

Ni	Cr	Mo	Fe	Nb	Co	Cu	Si, Mn	Al	Ti	C	P, S
50.00–55.00	17.00–21.00	2.80–3.30	Bal.	4.75–5.50	<1.00	<0.30	<0.35	0.20–0.80	0.65–1.15	<0.08	<0.015

2.2.1. Laser parameter optimization

A process window has been developed according to a newly published report, as shown in Fig. 9 [39]. A recession of good formability occurs as the laser power increases. Moreover, the distance covered by a better scanning speed and hatch spacing in the process window is narrowed under high laser power. With the proper choice of laser power, the relative densities of as-printed samples are all above 99.9%, as the volumetric energy density ranges from 83.33 to 117.64 J·mm^{-3} [39]. The smooth diffusion of Inconel 718 liquid is hindered by high viscosity at high scanning speed, thereby leading to the formation of openings. In the continuous scanning strategy, porosity increases sharply with increasing scanning speed. At the same time, it is shown that the molten pool is not deep enough to melt the front layer, resulting in the formation of under-fluidity viscous melts and a lack of melt flow, thus leading to the formation of arrays lacking a fusion hole [40].

The correlation between powder layer thickness and relative density has also been investigated. It has been found that strength properties are higher at a higher thickness owing to a reduction of porosity, although there is no direct evidence [41]. Yao *et al.* [42] optimized the process parameters and significantly improved relative density and surface smoothness, realizing the preparation of almost full density (>99.9% theoretical density) under 375 J/m linear energy density (defined as the ratio of laser power to scanning speed). Caiazzo *et al.* [43] fabricated Inconel 718 samples with densities of up to 99.97% and roughness below 1 μm by increasing volumetric energy density to 90 J·mm^{-3}. Zhang *et al.* [37] employed electrochemical polishing (ECP) to improve the surface quality of SLM Inconel 718 components and reduced surface roughness from 6.05 to 3.66 μm with 5 min of ECP.

2.2.2. Microstructure of as-printed and heat-treatment Inconel 718

The typical microstructure of SLM-prepared Inconel 718 is shown in Fig. 10 [44]. Due to a rapid solidification rate during the SLM process, columnar dendrites growing parallel to the construction direction can be clearly observed. The

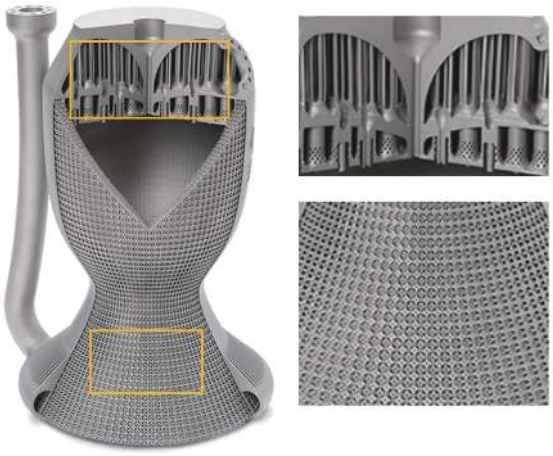

Fig. 8. Inconel 718 monolithic thrust chamber developed by CellCore GmbH and SLM Solutions, which directs the integration of multiple parts and internal features. The lattice structure accelerates cooling rate, reduces considerable weight, and increases stability [38].

matrix phase is γ phase, and the precipitates are mainly discoid γ″ phase (Ni_3Nb), spherical γ′ phase ($Ni_3(Al,Ti)$), needle flake δ phase (Ni_3Nb), dispersed MC, and island-like Laves phase [44].

As noted in Fig. 10(b)–(c), the Laves phase is an irregular island-like phase, which is formed by the segregation of niobium and other alloy elements in the matrix. Generally speaking, the Laves phase is the most destructive phase in SLM Inconel 718. A large number of irregular chain-like Laves phases are formed in the interbranch network, which needs to be dissolved by proper heat treatment [45]. Luo *et al.* [46] proposed that the precipitation of the Laves phases in a dendritic network might result from the formation of rich atomic clusters by niobium element micro-segregation, which may represent intermetallic phase nucleation sites at the end of solidification. Orthorhombic δ phase composed of Ni_3Nb always precipitates at grain boundaries in the form of needle flakes, which is not coherent with the matrix and usually reduces the plasticity of the material [47–48]. Double aging steps are supposed to control δ phase precipitation and promote γ″ and γ′ precipitation, as shown in Fig. 10(d).

Subsequent heat treatment is quite important for SLM Inconel 718 to dissolve the Laves phase, homogenize niobium element, reduce internal stress, and form strengthening γ′ and γ′′ phases. However, conventional heat treatment is somewhat improper for improving the microstructure and phase composition for additively manufactured Inconel 718 and should be adjusted [49].

Under low solution temperature, the Laves phase cannot be fully dissolved, nor can the segregation be homogenized. Meanwhile, grain coarsening and excess MC precipitation occur under long-duration and overly-high solution temperatures. Unreasonable aging treatment causes precipitation of δ phase instead of desired γ″ and γ′ phase, which has a certain positive effect on strength but significantly reduced ductility [50–53]. The most common heat treatment is "980°C/1040°C for 1 or 2 h solution, followed by 720°C for 8 h and 620°C for 10 h aging." Some studies add a homogenization step before solution treatment to acquire a more homogeneous microstructure. Compared with the aging treatment, the solution process has been discussed to confirm the best condition. Fig. 11 shows the evolution of microstructure of SLM Inconel 718 under different solution temperatures

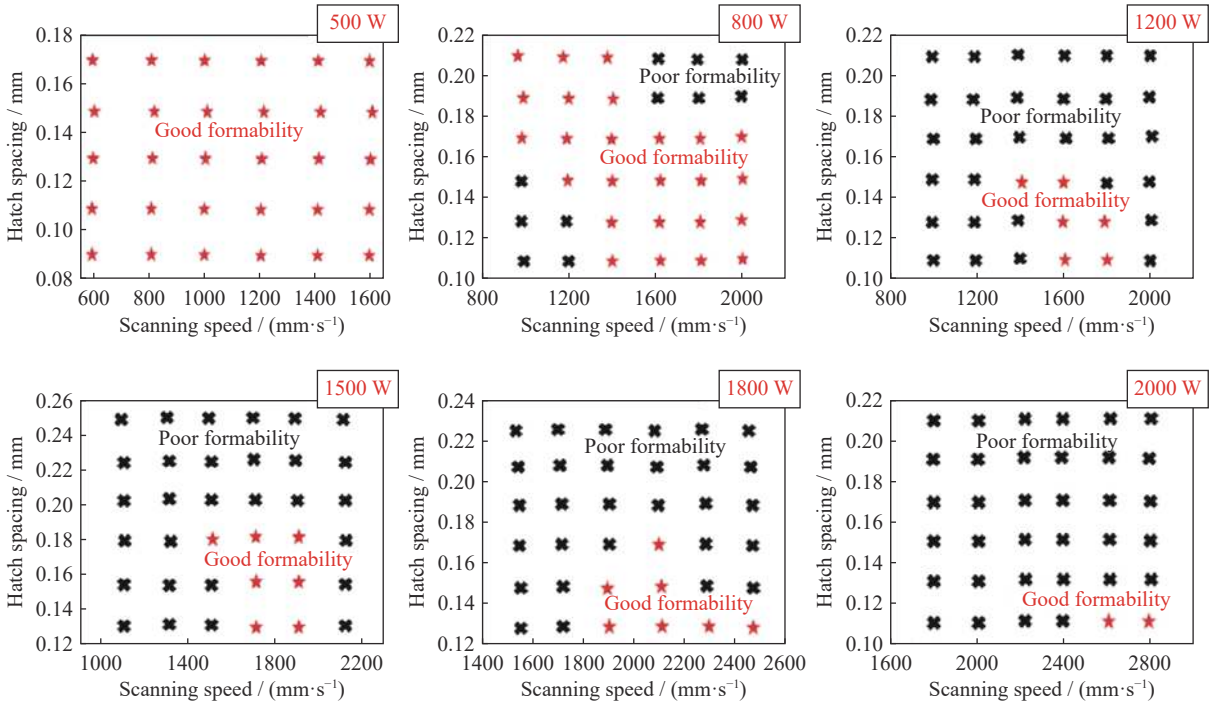

Fig. 9. Process windows of the Inconel 718 by SLM under laser power of 500 W, 800 W, 1200 W, 1500 W, 1800 W, and 2000 W. Reprinted from *J. Alloys Compd.*, 828, H.H. Yang, L. Meng, S.C. Luo, and Z.M. Wang, Microstructural evolution and mechanical performances of selective laser melting Inconel 718 from low to high laser power, 154473, Copyright 2020, with permission from Elsevier.

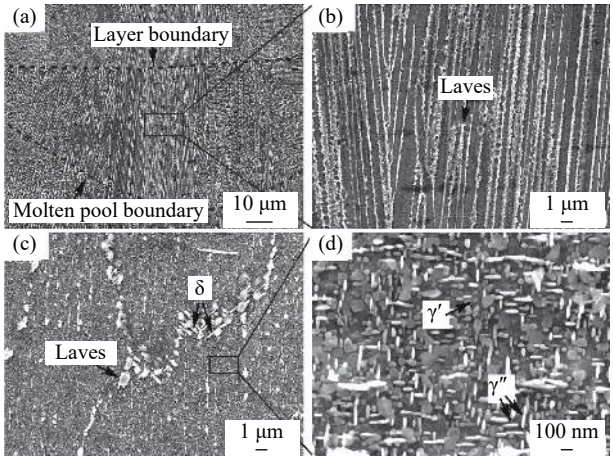

Fig. 10. SEM images of the as-printed Inconel 718 sample: (a) molten pool; (b) high-magnified micrograph of the columnar sub-structures. SEM images of SLM Inconel 718 samples after heat treatment: (c) precipitates at the grain boundaries and in the matrix; (d) magnified circular γ′ and disc-like γ″ phases. Reprinted from *J. Alloys Compd.*, 764, X. Li, J.J. Shi, C.H. Wang, G.H. Cao, A.M. Russell, Z.J. Zhou, C.P. Li, and G.F. Chen, Effect of heat treatment on microstructure evolution of Inconel 718 alloy fabricated by selective laser melting, 639-649, Copyright 2018, with permission from Elsevier.

(0°C, 980°C, 1040°C, and 1100°C, and aging at 720°C for 8 h and 620°C for 10 h designated as H0, H980, H1040, and H1100, respectively) and horizontal and vertical sections [54]. Average grain size increases with solution temperature while the fraction of low-angle grain boundaries (LAGBs) of the total grain boundaries (GBs) decreases. The fraction of the γ′ and γ″ phases increases from 24% to 45.5% after 980°C solution and double-step aging heat treatment, representing a clear improvement [54]. Huang *et al.* [55] believe that reducing solid solution treatment cooling rate is beneficial to raising the number of strengthening phases. Through a large number of experiments, they provided a quantitative relationship between the minimum solution time (t) and the solution temperature (T):

$$t = \frac{1}{3266}\exp\frac{21642}{T} \quad (1)$$

which is a basis for the selection of solid solution treatment parameters.

Seede *et al.* [56] studied the effect of heat treatment and HIP on the microstructure and, in particular, the texture of as-printed Inconel 718. A mixed equiaxed and columnar grain structure is obtained by homogenization heat treatment, associated with an approximate 15% reduction in texture. The (111) orientation in the vertical cross-sections remains prominent after both homogenization and HIP, while (002) orientation is reduced after homogenization and grows after HIP. Moreover, both treatments clearly promote the growth of grain boundary δ phase and MC-type brittle (Ti,Nb)C carbides. Seifi *et al.* [57] introduced HIP successfully to reduce defect density and translate columnar crystals to equiaxed ones on the basis of previous heat treatment. However, Tillmann *et al.* [58] pointed out that, although HIP can increase the density of as-printed components, it is almost impossible to obtain 100% density because a small amount of argon entrainment hinders full densification. All studies show that typical SLM microstructure basically disappears after HIP while grain size is significantly increased.

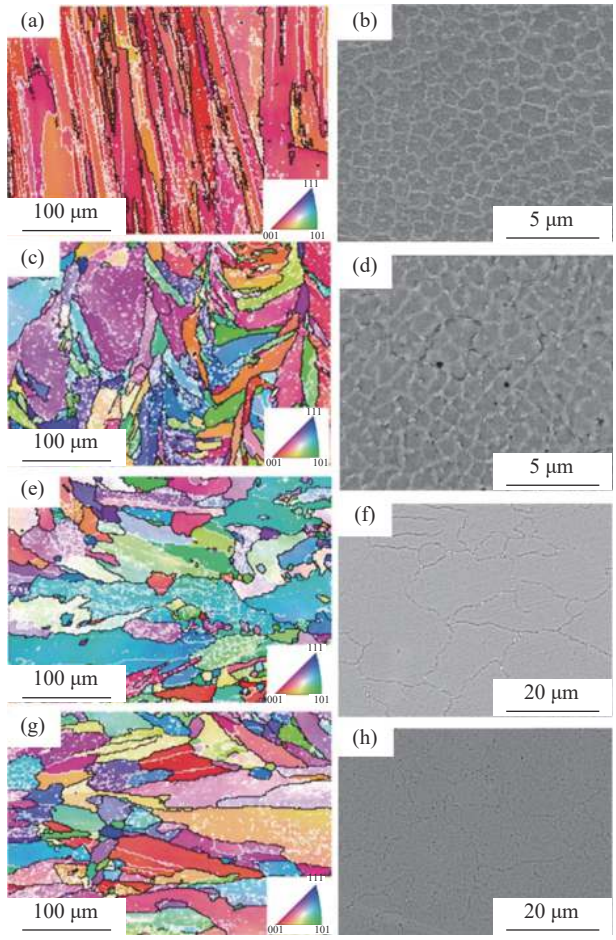

Fig. 11. Electron back-scattered diffraction (EBSD) inverse pole figure maps of as-printed samples after different temperature solution treatments: (a) H0, (c) H980, (e) H1040, (g) H1100; SEM images of as-printed samples after different temperature solution treatments: (b) H0, (d) H980, (f) H1040, (h) H1100. Reprinted from *Mater. Sci. Eng. A*, 748, M. Ni, S.C. Liu, C. Chen, R.D. Li, X.Y. Zhang, and K.C. Zhou, Effect of heat treatment on the microstructural evolution of a precipitation-hardened superalloy produced by selective laser melting, 275-285, Copyright 2019, with permission from Elsevier.

2.2.3. Mechanical property of as-printed and post-treatment Inconel 718

A summary of tensile properties of SLM-prepared Inconel 718 as reported in recent years is shown in Fig. 12 [41,51,54–55,57,59–64]. "SLMed" represents a specimen only fabricated by SLM without any post-treatment, "HT" represents a specimen with a solution treatment at 960–1130°C for 1 h and a double aging treatment at 720 and 620°C for 8–10 h after SLM, and "HIP" represents a specimen with HIP treatment and a double aging treatment after SLM.

The YS values of as-printed samples range from 643 to 873 MPa, increasing to 1100 MPa after HIP and to 1369 MPa after heat treatment. The UTS values of as-printed samples range from 940 to 1167 MPa, increasing to 1406 MPa after

HIP and to 1529 MPa after heat treatment. Both strength and ductility of as-printed specimens are almost equal to those of wrought specimens, but better than those of wrought specimens after HIP and heat treatment. Finer grains formed during the SLM process due to high cooling rates under high laser energy density play a major role. After solution, aging, or other heat treatment, mechanical properties of Inconel 718 can be further improved by second-phase precipitation and grain boundary strengthening. In addition, high-density dislocations and many LAGBs are produced due to a large temperature gradient. The results showed that the as-printed Inconel 718 without any post-processing treatment could also show excellent performance. However, the as-printed Inconel 718 contains part of the Laves phase in the interbranch region, which is harmful to the mechanical properties and must, in principle, be eliminated by heat treatment [46,59,65].

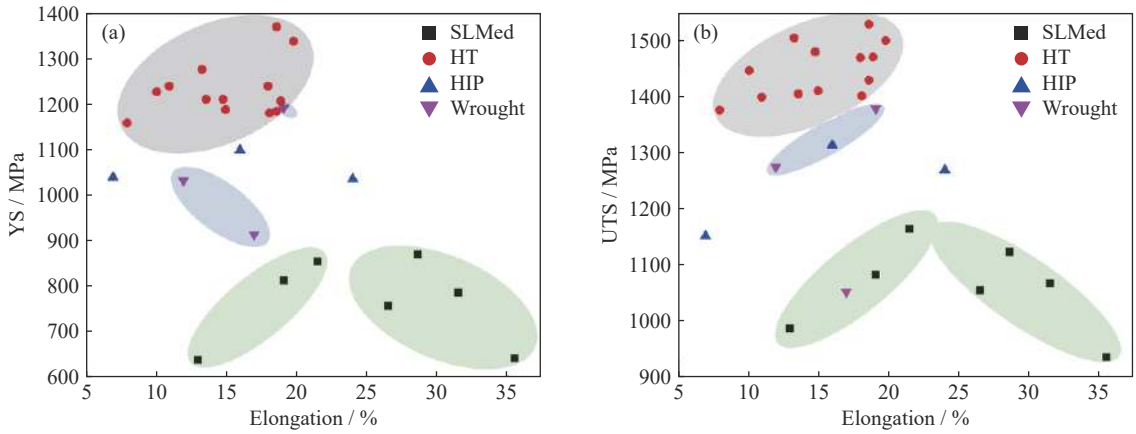

Fig. 12. Mechanical property profile of Inconel 718 fabricated by four processes. The black points represent as-printed samples, red points represent printed samples with solution treatment and double aging treatment, and blue points represent samples with HIP and double aging treatment. Correlation of YS and elongation is shown in (a), correlation of UTS and elongation is shown in (b). Both YS and UTS increase after heat treatment and HIP while elongation decreases (data from [41,51,54–55,57,59–64]).

It should be noted that the ductility of SLM samples after heat treatment or HIP decreases compared with as-printed samples, possibly owing to the elimination of cell structures and evolution of the δ phase [60]. Mechanical properties of as-printed samples depend on grain orientations, which is explained by the difference in accumulated residual stress and dislocation [61]. Moreover, it shows that dependence on orientation decreases after heat treatment due to the partial or complete residual stress elimination and dislocation recovery. Chlebus *et al.* [59] proposed that solid solution and double aging heat treatment are indispensable for as-printed Inconel 718 alloy. Homogenization temperature needs to be higher than the usual temperature (1100°C), and a slow furnace heating rate is required to avoid local subsolid liquation and possible propagation of metastable liquid along grain boundaries. In addition, it is pointed out that solid solution treatment cannot completely eliminate texture as elongation shape and orientation of grains still partly remain. Micro-segregation of niobium and titanium can be basically eliminated by a homogeneous or solution process but cannot be improved only by double aging treatment.

Mechanical properties of as-printed samples under different service temperatures have been compared with cast and wrought samples [62]. The tensile mechanical properties of printed samples (with standard heat treatment) are better than those of conventional samples at room temperature and at 450°C, but weaker than those of wrought samples at higher temperatures. This work showed that the YS, UTS, and elongation of printed samples are 1046 MPa, 1210 MPa and 13.7% at 450°C. However, when the tensile test is carried out at 650°C, the mechanical properties decrease significantly. The YS decreases to 862 MPa, UTS decreases to 1026 MPa, and elongation decreases to 7.9%.

Mechanical property variation along the building direction has been studied. Zhang *et al.* [66] characterized this along longitudinal directions in three 320 mm SLM printed cylinders with diameters of 5, 10, and 15 mm; the results are shown in Fig. 13(a). The ductility increases gradually along the building direction, while YS and UTS exhibit an opposite trend. Grain size increases along the building direction due to thermal history. γ″ phase distributes randomly in remelting regions while the Laves phase decreases from bottom to top due to a cooling rate decrease.

Fatigue properties of SLM-prepared Inconel 718 have also been evaluated [67]. The research showed that Inconel 718 prepared by SLM exhibits weak cyclic softening and significantly lower fracture strain, resulting in low fracture toughness. It is considered that the low fatigue property is related to low plastic toughness and unique micro-defects. The fatigue crack analysis shows (Fig. 13(b)) that the crack growth rate of the as-printed sample is much higher than that of wrought sample, while the experimental results show that the orientation of heterogeneous grains does not affect fatigue crack growth behavior.

3. Nickel-based superalloy strengthened by solid solution

Solid solution superalloy depends on lattice distortion caused by solute atoms. It can enhance strength and hardness

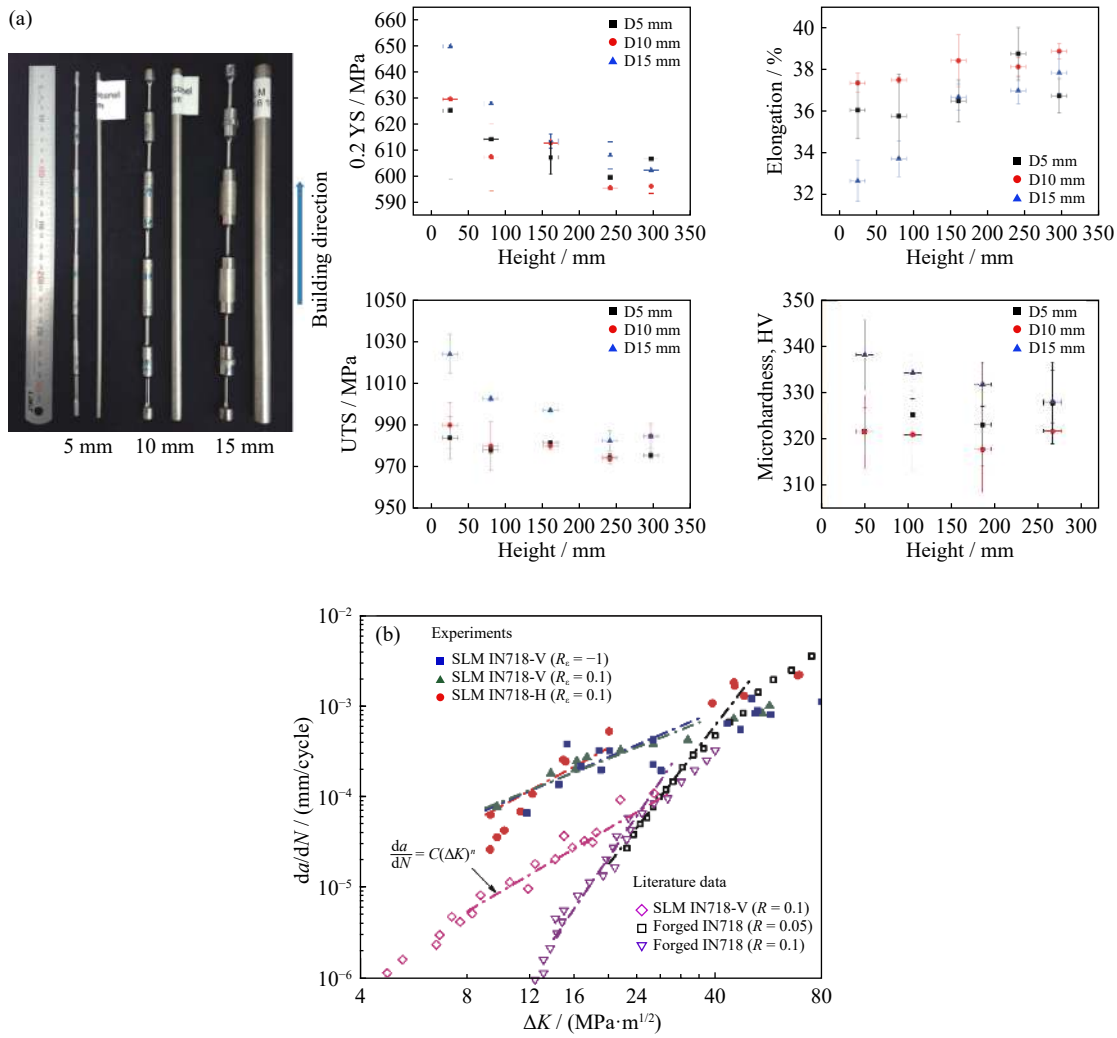

Fig. 13. (a) As-printed Inconel 718 cylindrical tensile specimens with different dimensions and UTS, YS, elongation, and microhardness evolution of those specimens along the building direction. (b) Comparison of fatigue crack growth rates of as-printed Inconel 718. 'V' and 'H' represent crack propagation in vertical and horizontal directions, respectively; d*a*/d*N* represents the crack growth rate; Δ*K* represents stress intensity factor range; *R* represents loading ratio in literature; R_ε represents loading ratio in literature. (a) is reprinted from *Mater. Sci. Eng. A*, 794, B.C. Zhang, P. Wang, Y. Chew, Y.J. Wen, M.H. Zhang, P. Wang, G.J. Bi, and J. Wei, Mechanical properties and microstructure evolution of selective laser melting Inconel 718 along building direction and sectional dimension, 139941, Copyright 2020, with permission from Elsevier; (b) is reprinted from *Mater. Sci. Eng. A*, 759, C.H. Pei, D. Shi, H. Yuan, and H.X. Li, Assessment of mechanical properties and fatigue performance of a selective laser melted nickel-base superalloy Inconel 718, 278-287, Copyright 2019, with permission from Elsevier.

owing to increasing resistance of dislocation gliding, making it difficult to slip. Inconel 625 and Hastelloy X are two main solid solution-strengthening nickel-based superalloys applied in SLM manufacturing. Both have attracted increasing attention and can serve above 850°C for long time spans; Hastelloy X can even serve up to 1080°C for a relatively short time. Different defects confront Hastelloy X and IN625 with different challenges during the SLM process, and the following section will introduce a comprehensive review of both superalloys.

3.1. Research progress of SLM Inconel 625 alloy (high service temperature)

The chemical composition of Inconel 625 is listed in Table 3 [68], where more than 50wt% of the chemical content is nickel, providing stable properties at elevated temperatures; over 20wt% is chromium, promoting resistance to oxidation and corrosion; both molybdenum and niobium are of significant contents, existing as solid solution atoms in the matrix [69]. Inconel 625 possesses the ability to serve within a broad use range from cryogenic temperature to 1000°C, and the ability to resist corrosion cracking resulting from chloride in harsh environments [70]. Inconel 625 appears as the solid solution superalloy with the greatest potential for SLM due to having few defects and stable high-temperature characteristics. However, Laves phases formed during the solidification process due to micro-segregation consume a large amount of Nb and Mo. In addition, localized thermoplastic deformation generates thermal residual stress in turn and may cause cracks and distortion of the final part. It is thus important to avoid the Laves phase and reduce residual stress during the SLM process.

Table 3. Chemical composition of Inconel 625 powder [68] wt%

Al	C	Co	Cr	Cb + Ta	Fe	Mn	Mo	Ni	P	S	Si	Ti
0.1	0.01	0.1	21.6	3.89	4.1	0.32	8.54	Bal.	0.015	0.015	0.28	0.2

3.1.1. Laser parameter optimization

Improper parameters result in defects and cause damage to mechanical properties. The introduction herein has introduced key parameters, but it should be noted that there are some differences between contour and hatching parameters in order to deal with edge and interior parts and raise density when printing Inconel 625. As shown in Fig. 14, open pores and micro-cracks are observed clearly [71]. Porosity mainly introduced by unmelted or partially melted particles still exists in SLM Inconel 625, although the density can be increased above 99% [72]. It is proved that width and depth of melt track increase with laser power and decrease with scanning speed. High laser power will cause a small contacting angle and high dynamics of the melt pool, which produce unmelted particles and pores more easily [68]. However, Koutiri *et al.* [73] found that high laser power is beneficial to improving surface quality, which also influences fatigue properties. Moreover, particles caused by spattering ejection and embedded in the surface and pores near the surface in the as-printed samples are considered as main crack initiation points and can be removed by polishing, thus achieving a lower surface roughness. Hence, a parameters scheme should be a compromise to acquire high density and good surface quality.

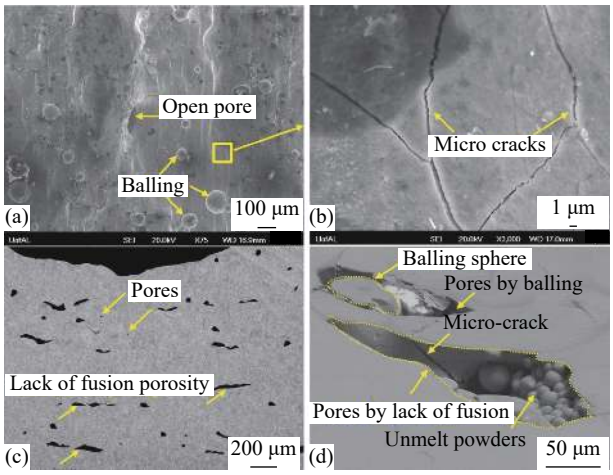

Fig. 14. SEM images of (a, b) as-printed Inconel 625 surface topography and (c, d) defects in the subsurface. Reprinted from *Mater. Sci. Eng. A*, 705, C. Li, R. White, X.Y. Fang, M. Weaver, and Y.B. Guo, Microstructure evolution characteristics of Inconel 625 alloy from selective laser melting to heat treatment, 20-31, Copyright 2017, with permission from Elsevier.

3.1.2. Microstructure of as-printed and post-solution treatment Inconel 625

The normal microstructure of Inconel 625 fabricated by SLM is shown in Fig. 15(a)–(c) [74]. A clear melting track is left on the top surface, and regular and constant molten pools, which are interconnected and V-shaped, are observed in the *Y*–*Z* cross section. The molten pool boundary can be found clearly under high magnification. In general, fine columnar crystal is formed inside the molten pool due to a high cooling rate that reaches 10^6 K/s. These columnar crystals have a strong crystallographic orientation along the build direction, which is proved by the EBSD picture as shown in Fig. 15(d) [75]. Meanwhile, high-density dislocation, residual stress, and low-angle boundary exist in the molten pool [68]. Fang *et al.* [76] investigated textures and grain boundary character distribution (GBCD) and verified that elongated columnar crystals grow across several layers and strong textures of <110> and <001> directions are generated, which are parallel to the build direction and scanning direction, respectively. {110} texture is more beneficial to GBCD, which is favorable for multiple twining. No precipitated phase and carbide are found in printed samples. Molybdenum and niobium atoms dissolve in the austenite matrix and cause a higher lattice constant.

SLM Inconel 625 usually needs solution treatment or HIP to release residual stress and reduce dislocation density. The solution treatment temperature should not be too high as solute atoms will precipitate from the matrix, and it is generally set from around 700 to 800°C to obtain an excellent integrated property. After solution treatment, grains inside the molten pool grow and transform into orthogonal textures. Meanwhile, fine grains form at the melt pool boundary, where foreign particles provide nucleation sites [74]. The hardness decreases as the release of residual stress when annealing at 700°C. In fact, niobium atoms will precipitate from the matrix and form γ″ phase (Ni_3Nb) combined with nickel atoms with a temperature above 600°C; therefore, lattice constant and strength decrease [75]. When annealing at 900°C, γ″ phase transforms into δ phase, which consumes numerous niobium atoms and leads to a further decrease in strength. However, when annealing temperature rises to 1000°C, a recovery in strength occurs, mainly because of the formation of a zigzag grain boundary with the precipitation of MC, which could improve strength and ductility. Fig. 15(e) shows a model of the segment of the grain boundary in the MC zone suggested by Li *et al.* [74]. HIP can increase density and strengthen the grain boundary so that samples treated with HIP possess high strength and elongation. Witkin *et al.* [77] also found {110} $\langle 01\bar{1} \rangle$ textures in samples annealing at 1150°C.

3.1.3. Mechanical property of as-printed and post-treatment Inconel 625

As shown in Fig. 16 [73,75,77–80], this section presents the strength and ductility of Inconel 625 samples fabricated by SLM from recent reports. Most tensile tests were carried out at room temperature. From the data, the strength of SLM-prepared Inconel 625 samples compares favorably with that of wrought samples at room temperature, although elongation is not particularly ideal. While heat treatment and HIP

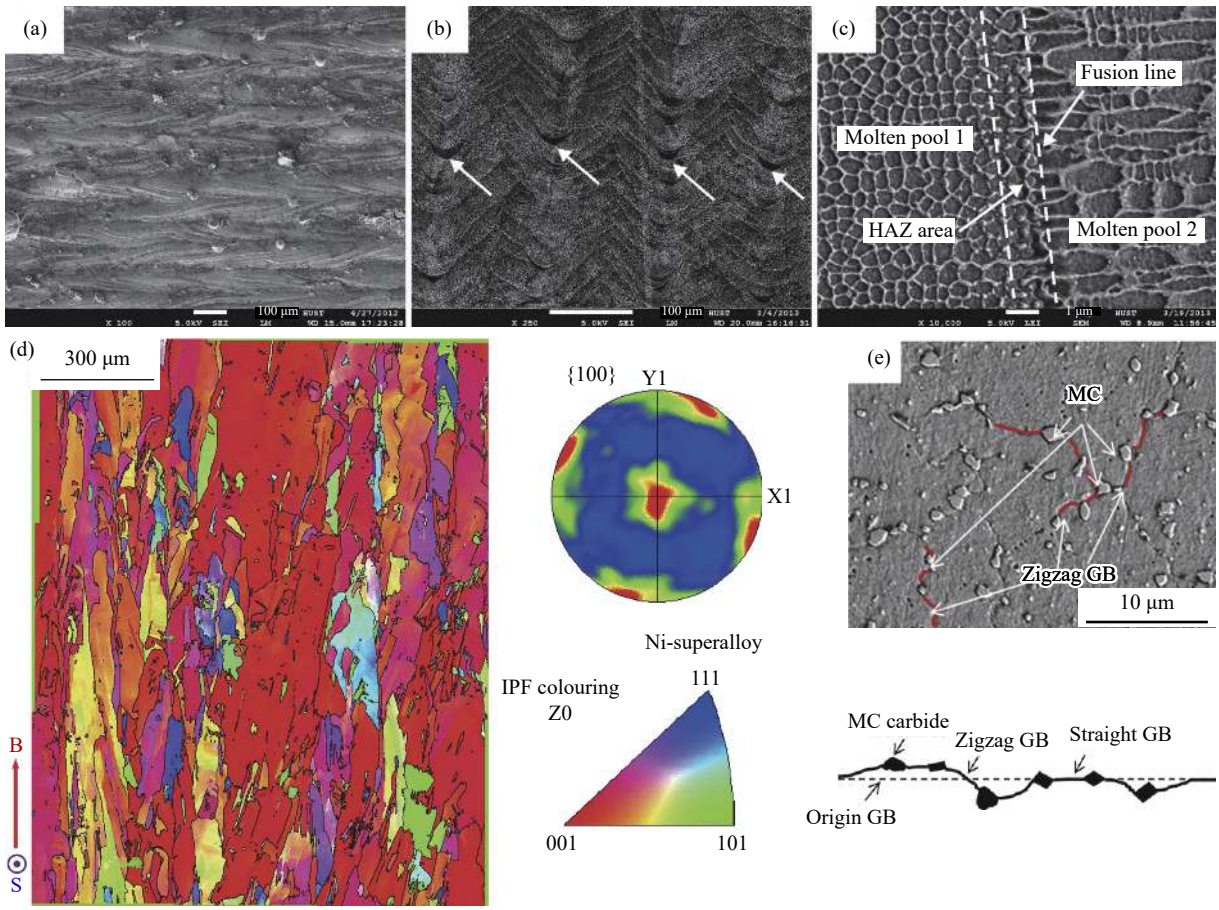

Fig. 15. SEM images of as-printed Inconel 625 samples: (a) top surface morphology, (b) "scales" shape of *Y–Z* section, (c) high magnification picture of the molten pool boundary. (d) EBSD analyses: Inverse pole figure-Z (IPF-Z) colored map of the *Y–Z* section and (100) pole figure where B stands for building direction and S for scanning direction. (e) SEM images of grain boundary structure and carbides and model of the segment of grain boundary in MC zone after heat treatment. (a), (b), (c), and (e) are reprinted from *J. Mater. Sci. Technol.*, 31, S. Li, Q.S. Wei, Y.S. Shi, Z.C. Zhu, and D.Q. Zhang, Microstructure characteristics of Inconel 625 superalloy manufactured by selective laser melting, 946-952, Copyright 2015, with permission from Elsevier; (d) is reprinted from *Mater. Sci. Eng. A*, 764, J. Nguejio, F. Szmytka, S. Hallais, A. Tanguy, S. Nardone, and M. Godino Martinez, Comparison of microstructure features and mechanical properties for additive manufactured and wrought nickel alloys 625, 138214, Copyright 2019, with permission from Elsevier.

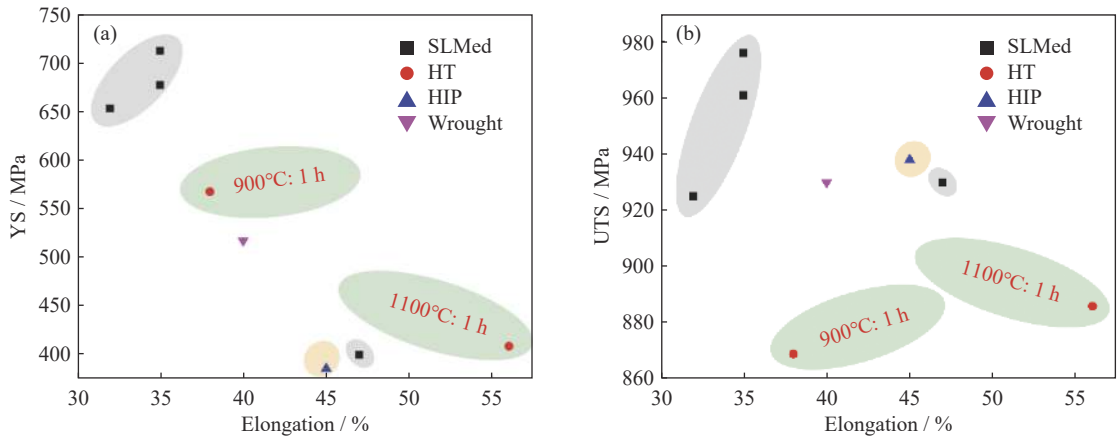

Fig. 16. Mechanical properties profile of Inconel 625 fabricated by four processes. The black points represent as-printed samples, red points represent printed samples with solution treatment, and blue points represent samples with HIP. Correlation of YS and elongation is shown in (a), correlation of UTS and elongation is shown in (b). Both YS and UTS decrease after heat treatment and HIP while elongation increases (data from [73,75,77–80]).

improve ductility due to a decrease in high dislocation density caused by residual stress, both YS and UTS partially decrease. However, when Hu *et al.* [78] conducted an experiment at 815°C, a sharp decrease in both strength and elonga-

tion occurred at elevated temperatures where wrought samples maintained good ductility, meaning that high-temperature mechanical properties of SLM-prepared Inconel 625 need improvement. The poor ductility at elevated temperatures may have been caused by precipitation of carbide, making the grain boundary more easily broken and aggravating brittleness. Some studies have worked on improving mechanical properties by annealing treatment or HIP, yet it seems insurmountable to increase strength and elongation at the same time. In fact, a compromise between strength and plasticity is important.

The grain boundary is destroyed and cracking occurs because of inconsonant deformation among grains in the heterogeneous parts [78]. Pores and unmelted particles cause micro-cracking, and, in turn, joint cracking causes breakage. Ductile fracture is uncommon, while the brittle fracture is observed in most reports. In addition to these conventional studies, some innovative works have been carried out. Leary *et al.* [81] fabricated complex Inconel 625 lattice structure components by SLM, which exhibited good ductility. Mumtaz and Hopkinson [82] attempted to use a pulse laser to optimize the SLM process for manufacturing IN625 components. It is believed that more investigations will focus on the fundamental mechanism of SLM-formed Inconel 625 and the cutting-edge technology that could be introduced to this process.

3.2. Research progress of SLM Hastelloy X alloy (service temperature below 900°C)

Hastelloy X is a typical solution-strengthening nickel-based superalloy strengthened mainly by molybdenum and tungsten atoms, which can serve at 900°C for an extended time, with excellent corrosion resistance and mechanical properties [83]. Only in recent years crack and density have been controlled to an acceptable level. With advanced SLM technology and the development of mature commercial Hastelloy X powder for the SLM process, Hastelloy X components fabricated by SLM have shown great promise for the aerospace industry, while it is unpromising for AM due to poor weldability. Researchers have focused much effort on avoiding cracks during the SLM process, not only through optimizing parameters but also through adjusting the chemical composition of the powder, including reducing the content of carbon and silicon. Sanchez-Mata *et al.* [84] manufactured crack-free Hastelloy X components using commercial powder provided by LPW Technology Ltd. and a Renishaw AM400 machine. The chemical composition of this powder and another provided by Oerlikon are shown in Table 4. Currently, researchers have focused on the correlation between microstructure and mechanical properties as well as the effect of post-treatment. Some commercial attempts have been made, including by Siemens, which cooperated with EOS to redesign burner fronts featuring functional integration using Hastelloy X and SLM [85].

3.2.1. Laser parameter optimization

Hot tearing and cold tearing are two chief causes of crack generation in Hastelloy X prepared by SLM. The former causes micro-cracks during the process of solidification due to the existence of minor elements, a larger solidification temperature range, and a reduced eutectic phase. The latter causes cracks when alloys solidify completely due to huge residual stresses introduced by repeated thermal cycles. It is recognized that cracks originate from grain boundaries, extend to molten pool boundaries, and across the molten pool, spreading along new grain boundaries [86]. Different methods for eliminating cracks need to be determined according to the different mechanisms of crack generation. Laser parameter optimization is effective in eliminating cracks caused by cold tearing, as shown in Fig. 17, where Montero-Sistiaga *et al.* [87] have produced crack-free SLM Hastelloy X components (using a modified commercial variant of Hastelloy X powder provided by Oerlikon AM). However, residual stresses introduced by repeated thermal cycles cannot result in cracks individually, meaning micro-cracks generated during the process of solidification are prime and the redesign of the powder chemical composition is indispensable, as reported by Tomus *et al.* [86]. The same conclusion was drawn by Harrison *et al.* [88]. They believe the fundamental method is to promote thermal shock resistance of the material by increasing the content of solid solution atoms to form a supersaturated solid solution and increasing lattice stress on the condition of rapid solidification rates of SLM, which can improve tensile properties at the same time.

Table 4. Chemical compositions of two Hastelloy X powders for SLM wt%

Provider	Ni	Cr	Fe	Mo	Co	W	Mn	Si	C
LPW Technology Ltd.	Bal.	21.2	17.6	8.8	2.0	NW	<0.1	0.2	0.06
Oerlikon	Bal.	20.5–23.0	17.0–20.0	8.0–10.0	0.5–2.5	0.2–1.0	<0.1	<1.0	<0.15

Note: NW—No mark.

Another task for parameter optimization is to increase density. Tomus *et al.* [89] found that the density of as-printed samples increases as scanning speed decreases. When the scanning speed is too fast, laser energy is not adequate for melting powder completely. Molten pools and pores are generated. In response, this team successfully increased the density of samples from 77% to 99% by properly reducing scanning speed and forming continuous molten pools. As shown in Fig. 17(b), components possess a density of over 99% when the volumetric energy density reaches above 50 $J \cdot mm^{-3}$. Montero-Sistiaga *et al.* [90] observed the same phenomenon and further investigated the effect of laser power on density. They found low laser power under high volumetric energy density can cause key-hole pores and reduce the density of the material. Calignano and Minetola [91] produced samples with densities of up to 99.88% (laser power: 195 W;

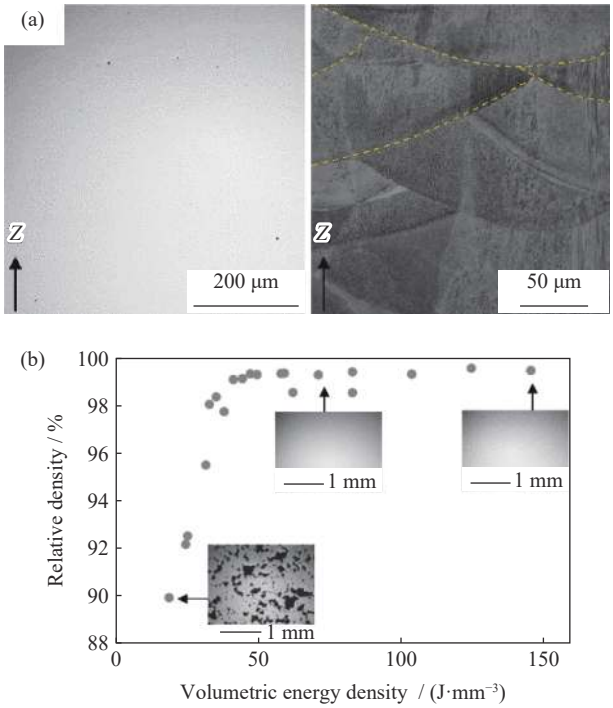

Fig. 17. (a) SEM images of as-printed Hastelloy X polished cross section and etched microstructure along the building direction. (b) Relative density of as-printed Hastelloy X as a function of the volumetric energy. The top two images show full dense samples, while the bottom image shows unmelted regions in black. Reprinted from *Addit. Manuf.*, 31, M.L. Montero-Sistiaga, Z.Z. Liu, L. Bautmans, S. Nardone, G. Ji, J.P. Kruth, J. Van Humbeeck, and K. Vanmeensel, Effect of temperature on the microstructure and tensile properties of micro-crack free Hastelloy X produced by selective laser melting, 100995, Copyright 2020, with permission from Elsevier.

scanning speed: 1000 mm/s; hatch spacing: 0.05 mm; layer thickness: 0.02 mm). Their result was achieved through observation of porosity on optical images; other teams may have ignored micropores, thus introducing errors. More precise methods, such as CT, should be employed to detect density.

3.2.2. Microstructure of as-printed and post-treatment Hastelloy X

The microstructure of as-printed samples exhibits typical SLM-prepared features with a fine grain size due to a rapid cooling/solidification rate. Stacked molten pools are observed at longitudinal sections. The epitaxially grown grains exist as columnar crystals and form a texture that is longer than the depth of one molten pool. The orientation of columnar crystal is the same in molten pools between alternating layers, and different in adjacent molten pools. However, there is a divergence if MC precipitation exists in the as-printed samples.

According to Montero-Sistiaga *et al.* [87], molten pool boundaries can be observed clearly after heat treatment at 800°C for 2 h, but they disappear when the temperature increases to 1177°C (a standard heat-treatment temperature for Hastelloy X). Grain size and morphology cannot be changed after both heat treatments, meaning no recrystallization. The texture of <100> along the building direction is retained, although the high density of dislocations decreases after heat treatment. These kinds of precipitation are detected in 800°C samples, including those of Mo-rich M_6C, Cr-rich $M_{23}C$, and needle-shaped Mo-rich topologically close-packed (TCP) μ phase. The change in dislocations and precipitation are shown in TEM images in Fig. 18(a)–(d). Li *et al.* [92] also found MC precipitation in samples after HIP, and TEM showed their diameter to be approximately 100 nm in grain boundaries and within grains. It is generally assumed that MC plays an important role in mechanical properties, while Tomus *et al.* [93] believe MC has virtually no influence; they claim the content of carbon is too low to make a difference.

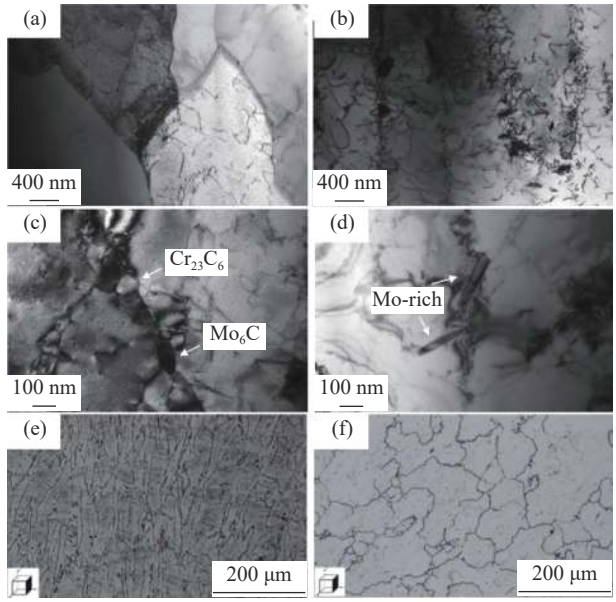

Fig. 18. TEM images of as-printed Hastelloy X after heat treatment at (a) 1177°C and (b–d) 800°C for 2 h. Two types of carbide are found at intergranular and intragranular regions, and needle-shaped phases are found within the grains. Grain morphology SEM images of as-printed Hastelloy X after HIP at (e) 1100°C/160 MPa/2 h and (f) 1175°C/160 MPa/2 h [92]. (a–d) are reprinted from *Addit. Manuf.*, 31, M.L. Montero-Sistiaga, Z.Z. Liu, L. Bautmans, S. Nardone, G. Ji, J.P. Kruth, J. Van Humbeeck, and K. Vanmeensel, Effect of temperature on the microstructure and tensile properties of micro-crack free Hastelloy X produced by selective laser melting, 100995, Copyright 2020, with permission from Elsevier.

HIP is carried out to close cracks and pores. Li *et al.* [92] performed HIP under 1100 and 1175°C at the same pressure and time. Grains coarsened and recovery occurred during HIP at both temperatures. However, the texture was maintained at 1100°C, while columnar crystal transformed into equiaxed crystal under 1175°C, as shown in Fig. 18(e)–(f). In addition, the amount of MC was reduced, and the size of MC within the grain increased to 3 μm after HIP at 1175°C. HIP is a thermal activation process that enhances grain boundary migration and grain growth, indicating the growth of grains might lead to a reduction in MC. However, Toumos *et al.* [93] found the size and amount of MC do not change while it tends to precipitate along the grain boundary.

3.2.3. Mechanical property of as-printed and post-treatment Hastelloy X

Some teams have reported the mechanical properties of Hastelloy X components fabricated by SLM, including as-printed samples and samples after post-treatment at room temperature and elevated temperature. Unfortunately, specific data for strength and elongation are not listed in most literature, so we cannot conclude quantitatively as Inconel 718 and Inconel 625. As shown in Fig. 19(a), the strength of as-printed samples is superior to those of wrought samples due to fine grain size, high density of dislocation, and supersaturated solid solution [94]. However, the elongation of as-printed samples is lower than that of wrought samples. There is still a gap despite improvement in plasticity by HIP.

Cracks and other defects cause premature failure of SLM samples at room temperature. Except for micro-cracks induced during the SLM process, molten pool boundaries, which contact each other at different angles, can become initial points of new cracks under loading. Molten pool boundaries between alternating layers possess better ductility and tend toward ductile deformation, while adjacent molten pool boundaries tend toward plastic deformation. Horizontal and vertical samples exhibit differences in deformation behavior due to different grain orientations [93]. As shown in Fig. 19(b), grains of vertical samples are elongated along the loading direction, while grains of horizontal samples are

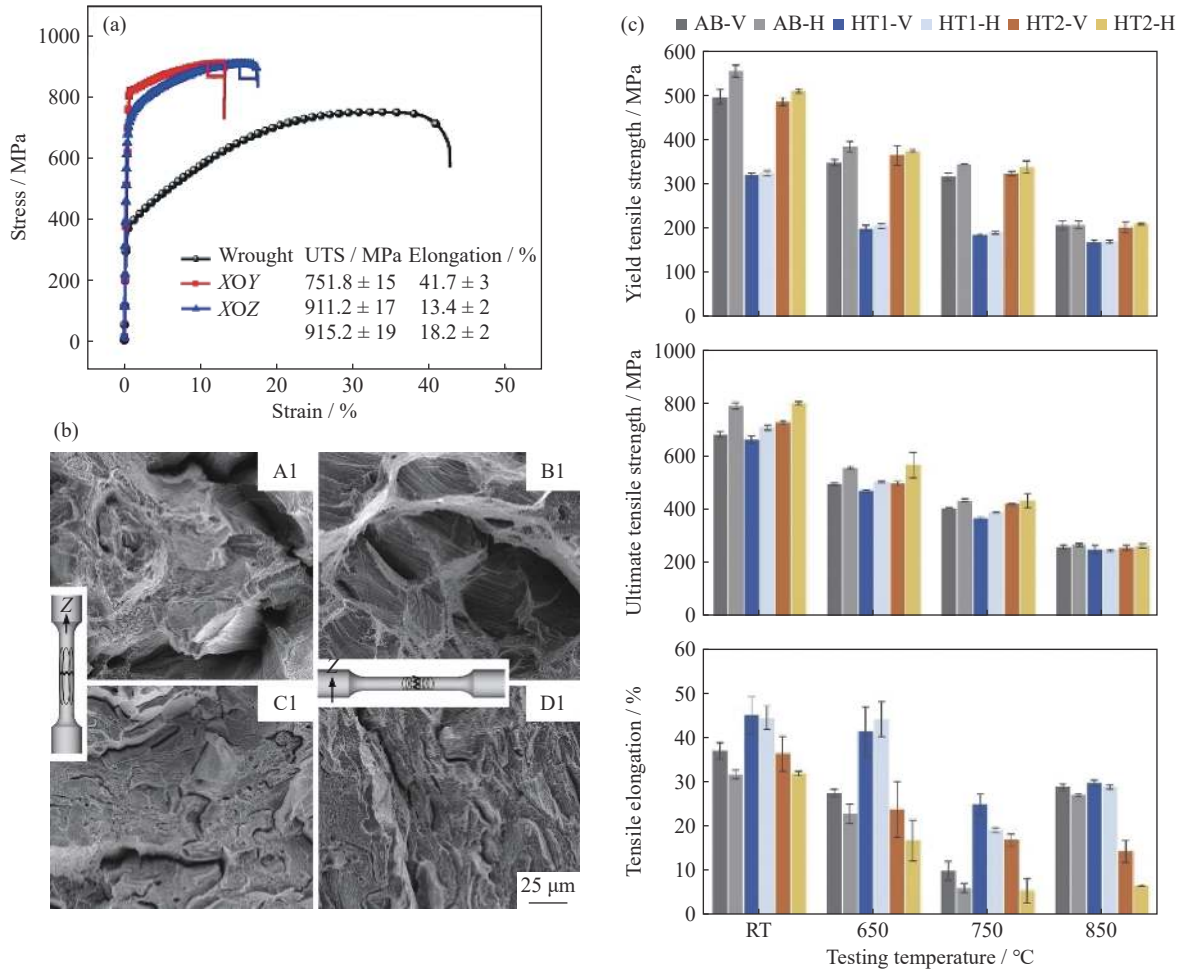

Fig. 19. (a) Engineering stress vs. strain responses of wrought and as-printed Hastelloy X on different planes. (b) SEM images of fracture surfaces for as-printed samples (A1 and B1) and samples after HIP (C1 and D1). Vertically built samples are shown in A1 and C1, horizontally built samples are shown in B1 and D1. The insets show the relationship between tensile sample geometry, loading direction, SLM building direction *Z* and fracture surface from where the images were taken. (c) Tensile results of different as-printed (AB) samples built in the horizontal (H) and vertical (V) directions and samples after different heat treatments: HT1 (1177°C/2 h) and HT2 (800°C/2 h) at different testing temperatures: room temperature (RT), 650°C, 750°C and 850°C. (a) is reprinted from *Constr. Build. Mater.*, 221, D.C. Kong, X.Q. Ni, C.F. Dong, L. Zhang, J.Z. Yao, C. Man, L. Wang, K. Xiao, and X.G. Li, Anisotropic response in mechanical and corrosion properties of Hastelloy X fabricated by selective laser melting, 720-729, Copyright 2019, with permission from Elsevier; (b) is reprinted from *Mater. Sci. Eng. A*, 667, D. Tomus, Y. Tian, P.A. Rometsch, M. Heilmaier, and X.H. Wu, Influence of post heat treatments on anisotropy of mechanical behaviour and microstructure of Hastelloy-X parts produced by selective laser melting, 42-53, Copyright 2016, with permission from Elsevier; (c) is reprinted from *Addit. Manuf.*, 31, M.L. Montero-Sistiaga, Z.Z. Liu, L. Bautmans, S. Nardone, G. Ji, J.P. Kruth, J. Van Humbeeck, and K. Vanmeensel, Effect of temperature on the microstructure and tensile properties of micro-crack free Hastelloy X produced by selective laser melting, 100995, Copyright 2020, with permission from Elsevier.

broken plastic perpendicular to the loading direction. It can be observed that the surface of the as-printed sample is a mixture of dimples and cleavage-type fractures, but only dimples exist on the surface of samples after HIP and heat treatment. As mentioned above, HIP and heat treatment can both reduce the density of dislocation, although they result in a decrease in strength. HIP coarsens grains and closes pores when increasing elongation, and HIP plus heat treatment can promote the formation of dimples and improve ductility.

When a tensile test is operated at elevated temperatures, the effect of MC precipitation becomes important. As shown in Fig. 19(c), elongation of all samples decreases at 750°C due to the formation of MC, which is a brittle phase precipitating at grain boundaries. Montero-Sistiaga *et al.* [87] confirmed the formation temperature of MC is approximately 700°C and dissolution temperature is approximately 850°C by confocal scanning laser microscopy. There is a significant amount of MC in 800°C samples while MC dissolved at 1177°C samples. Therefore, the strength of 800°C samples is comparable to as-printed samples, although dislocation is reduced. The elongation of all samples rises again at 850°C with the dissolution of MC. Kong *et al.* [94] hold the same opinion: MC can increase strength but decrease ductility as it is brittle and maintains a different deformation rate within the matrix.

Other research has also been performed. Tian *et al.* [95] investigated the influence of SLM parameters on surface roughness by statistical methods and predicted surface roughness values coincident with experimental results through predicted equations. Han *et al.* [96] studied the compressive property of lattice structures for the first time. More work will be undertaken as Hastelloy has great potential.

4. Conclusions and future scopes

Based on this review, the SLM process for nickel-based superalloy has been discussed by illustrating representative alloys. The main process obstacles of SLM-prepared nickel-based superalloys include avoiding cracks and increasing density, improving ductility, and maintaining high strength. However, different enterprises should be noted at the same time. Chemical composition is predominant for CM247LC and Hastelloy X, which are more sensitive to cracks. The establishment of a process window is the next goal for Inconel 625, and more effort should be devoted to accelerating industrialization for Inconel 718. The following is the future scope of study in terms of the current focus of researchers:

(1) Expanding the application range of materials. It is difficult for most nickel-based superalloys to be manufactured by SLM, so chemical composition modification for conventional material is needed to expand the materials' application range. More fundamentally, alloy design for SLM is the final method to avoid cracks rather than relying only on parameter optimization. The development of customized nickel-based superalloys is an indispensable step.

(2) Nano-additive to improve stability. Metal matrix composite has been popular in recent years; some nano-additives such as graphene nanoplatelets are added to the metallic materials to improve their properties, especially strength. One team has reported successfully fabricating IN718 with graphene nanoplatelets WC particles by SLM [97]. Those components presented satisfactory progress in mechanical properties.

(3) Assessment of mechanical properties at elevated temperature. It should be noted that, in particular, a great majority of mechanical tests reported in the literature were executed at room temperature, while nickel-based superalloy served at elevated temperatures. The high temperature will trigger *in-situ* solid-state phase transformation. The microstructure evolution and deformation mechanism for SLM-prepared nickel-based superalloy need urgent clarification.

Clearly, some fundamental physical phenomena have not been completely understood, such as interaction among laser, metal powder, and molten pool, even for Inconel 718, which has received the most attention. Further progress has been established in SLM machines and material characterization methods. The former ensures the stability of products and the latter helps in revealing basic theory. However, commercial demand has been increasing in spite of this. It is reported that the European Space Agency executed a test of a full-scale 3D manufactured rocket engine demonstrator-BERTA in 2019, for which a nozzle adopted SLM-prepared nickel-based superalloy [98]. Boeing, Lockheed Martin, Airbus, and other giant companies all increased investment in 3D printing metal material. As people continue to explore space and manufacturing upgrades to integration, SLM-prepared nickel-based superalloy will boom in the following decades.

Acknowledgements

This work was financially supported by the National Natural Science Foundation of China (No. 51901020), Shandong Key Research and Development Plan Project (No. 2019JZZY010327), Aeronautical Science Foundation of China (No. 201942074001), and the Fundamental Research Funds for the Central Universities, University of Science and Technology Beijing (No. FRF-IP-20-05).

Conflict of Interest

The authors declare that they have no known competing interests or personal relationships that could have appeared to influence the work reported in this paper.

References

[1] R.C. Reed, *The Superalloys: Fundamentals and Applications*, Cambridge University Press, Cambridge, 2006.

[2] S.L. Chittewar and N.G. Patil, Surface integrity of conventional and additively manufactured nickel superalloys: A review, *Mater. Today: Proc.*, 44(2021), p. 701.

[3] S. Sanchez, P. Smith, Z.K. Xu, G. Gaspard, C.J. Hyde, W.W. Wits, I.A. Ashcroft, H. Chen, and A.T. Clare, Powder bed fu-

sion of nickel-based superalloys: A review, *Int. J. Mach. Tools Manuf.*, 165(2021), art. No. 103729.
[4] Rolls-Royce, *The Jet Engine*, The Technical Publications Department, Derby, 1992.
[5] N.A. Cumpsty, *Jet Propulsion: A Simple Guide to the Aerodynamic and Thermodynamic Design and Performance of Jet Engines*, Cambridge University Press, Cambridge, 1997.
[6] H.Y. Wu, D. Zhang, B.B. Yang, C. Chen, Y.P. Li, K.C. Zhou, L. Jiang, and R.P. Liu, Microstructural evolution and defect formation in a powder metallurgy nickel-based superalloy processed by selective laser melting, *J. Mater. Sci. Technol.*, 36(2020), p. 7.
[7] X.P. Du and J.C. Zhao, First measurement of the full elastic constants of Ni-based superalloy René 88DT, *Scripta Mater.*, 152(2018), p. 24.
[8] S.H. Sun, Y. Koizumi, T. Saito, K. Yamanaka, Y.P. Li, Y.J. Cui, and A. Chiba, Electron beam additive manufacturing of Inconel 718 alloy rods: Impact of build direction on microstructure and high-temperature tensile properties, *Addit. Manuf.*, 23(2018), p. 457.
[9] W.E. Frazier, Metal additive manufacturing: A review, *J. Mater. Eng. Perform.*, 23(2014), No. 6, p. 1917.
[10] J.J. Lewandowski and M. Seifi, Metal additive manufacturing: A review of mechanical properties, *Annu. Rev. Mater. Res.*, 46(2016), No. 1, p. 151.
[11] H.Y. Chen, D.D. Gu, Q. Ge, X.Y. Shi, H.M. Zhang, R. Wang, H. Zhang, and K. Kosiba, Role of laser scan strategies in defect control, microstructural evolution and mechanical properties of steel matrix composites prepared by laser additive manufacturing, *Int. J. Miner. Metall. Mater.*, 28(2021), No. 3, p. 462.
[12] Y.W. Luo, M.Y. Wang, J.G. Tu, Y. Jiang, and S.Q. Jiao, Reduction of residual stress in porous Ti_6Al_4V by *in situ* double scanning during laser additive manufacturing, *Int. J. Miner. Metall. Mater.*, 28(2021), No. 11, p. 1844.
[13] L.N. Carter, C. Martin, P.J. Withers, and M.M. Attallah, The influence of the laser scan strategy on grain structure and cracking behaviour in SLM powder-bed fabricated nickel superalloy, *J. Alloys Compd.*, 615(2014), p. 338.
[14] W.H. Yu, S.L. Sing, C.K. Chua, C.N. Kuo, and X.L. Tian, Particle-reinforced metal matrix nanocomposites fabricated by selective laser melting: A state of the art review, *Prog. Mater. Sci.*, 104(2019), p. 330.
[15] I. Yadroitsev, P. Bertrand, and I. Smurov, Parametric analysis of the selective laser melting process, *Appl. Surf. Sci.*, 253(2007), No. 19, p. 8064.
[16] D.D. Gu, W. Meiners, K. Wissenbach, and R. Poprawe, Laser additive manufacturing of metallic components: Materials, processes and mechanisms, *Int. Mater. Rev.*, 57(2012), No. 3, p. 133.
[17] D. Wang, Z.Y. Qian, W.H. Dou, Y.Q. Yang, S. Li, Y.C. Bai, and Z.F. Xiao, Research progress on selective laser melting of nickel based superalloy, *Addit. Manuf. Technol.*, 61(2018), No. 10, p. 49.
[18] R.W. Kozar, A. Suzuki, W.W. Milligan, J.J. Schirra, M.F. Savage, and T.M. Pollock, Strengthening mechanisms in polycrystalline multimodal nickel-base superalloys, *Metall. Mater. Trans. A*, 40(2009), No. 7, p. 1588.
[19] K. Kunze, T. Etter, J. Grässlin, and V. Shklover, Texture, anisotropy in microstructure and mechanical properties of IN738LC alloy processed by selective laser melting (SLM), *Mater. Sci. Eng. A*, 620(2015), p. 213.
[20] P. Kanagarajah, F. Brenne, T. Niendorf, and H.J. Maier, Inconel 939 processed by selective laser melting: Effect of microstructure and temperature on the mechanical properties under static and cyclic loading, *Mater. Sci. Eng. A*, 588(2013), p. 188.
[21] Z. Chen, S.G. Chen, Z.Y. Wei, L.J. Zhang, P. Wei, B.H. Lu, S.Z. Zhang, and Y. Xiang, Anisotropy of nickel-based superalloy K418 fabricated by selective laser melting, *Prog. Nat. Sci.*, 28(2018), No. 4, p. 496.
[22] Z.H. Jiao, L.M. Lei, H.C. Yu, F. Xu, R.D. Xu, and X.R. Wu, Experimental evaluation on elevated temperature fatigue and tensile properties of one selective laser melted nickel based superalloy, *Int. J. Fatigue*, 121(2019), p. 172.
[23] W.P. Huang, H.C. Yu, J. Yin, Z.M. Wang, and X.Y. Zeng, Microstructure and mechanical properties of k4202 cast nickel base superalloy fabricated by selective laser melting, *Acta Metall. Sin.*, 52(2016), No. 9, p. 1089.
[24] S.E. Atabay, O. Sanchez-Mata, J.A. Muñiz-Lerma, R. Gauvin, and M. Brochu, Microstructure and mechanical properties of rene 41 alloy manufactured by laser powder bed fusion, *Mater. Sci. Eng. A*, 773(2020), art. No. 138849.
[25] Z. Qiao, C. Li, H.J. Zhang, H.Y. Liang, Y.C. Liu, and Y. Zhang, Evaluation on elevated-temperature stability of modified 718-type alloys with varied phase configurations, *Int. J. Miner. Metall. Mater.*, 27(2020), No. 8, p. 1123.
[26] L.N. Carter, M.M. Attallah, and R.C. Reed, Laser powder bed fabrication of nickel-base superalloys: Influence of parameters; characterisation, quantification and mitigation of cracking, [in] E.S. Huron, R.C. Reed, M.C. Hardy, M.J. Mills, R.E. Montero, P.D. Portella, J. Telesman, eds., *Superalloys 2012*, John Wiley & Sons, Inc., Hoboken, 2012, p. 577.
[27] K. Harris, G.L. Erickson, and R.E. Schwer, MAR M 247 derivations - CM 247 LC DS alloy and CMSX single crystal alloys: Properties & performance, [in] *Proceedings of the fifth International Symposium on Superalloys*, Warrendale, PA, 1984, p. 221.
[28] M.B. Henderson, D. Arrell, R. Larsson, M. Heobel, and G. Marchant, Nickel based superalloy welding practices for industrial gas turbine applications, *Sci. Technol. Weld. Joining*, 9(2004), No. 1, p. 13.
[29] S. Catchpole-Smith, N. Aboulkhair, L. Parry, C. Tuck, I.A. Ashcroft, and A. Clare, Fractal scan strategies for selective laser melting of 'unweldable' nickel superalloys, *Addit. Manuf.*, 15(2017), p. 113.
[30] R.P. Turner, C. Panwisawas, Y. Lu, I. Dhiman, H.C. Basoalto, and J.W. Brooks, Neutron tomography methods applied to a nickel-based superalloy additive manufacture build, *Mater. Lett.*, 230(2018), p. 109.
[31] N. Kalentics, N. Sohrabi, H.G. Tabasi, S. Griffiths, J. Jhabvala, C. Leinenbach, A. Burn, and R.E. Logé, Healing cracks in selective laser melting by 3D laser shock peening, *Addit. Manuf.*, 30(2019), art. No. 100881.
[32] G. Bidron, A. Doghri, T. Malot, F. Fournier-Dit-chabert, M. Thomas, and P. Peyre, Reduction of the hot cracking sensitivity of CM-247LC superalloy processed by laser cladding using induction preheating, *J. Mater. Process. Technol.*, 277(2020), art. No. 116461.
[33] X.Q. Wang, L.N. Carter, B. Pang, M.M. Attallah, and M.H. Loretto, Microstructure and yield strength of SLM-fabricated CM247LC Ni-superalloy, *Acta Mater.*, 128(2017), p. 87.
[34] V.D. Divya, R. Muñoz-Moreno, O.M.D.M. Messé, J.S. Barnard, S. Baker, T. Illston, and H.J. Stone, Microstructure of selective laser melted CM247LC nickel-based superalloy and its evolution through heat treatment, *Mater. Charact.*, 114(2016), p. 62.
[35] R. Muñoz-Moreno, V.D. Divya, S.L. Driver, O.M.D.M. Messé, T. Illston, S. Baker, M.A. Carpenter, and H.J. Stone, Effect of heat treatment on the microstructure, texture and elastic anisotropy of the nickel-based superalloy CM247LC processed by selective laser melting, *Mater. Sci. Eng. A*, 674(2016), p. 529.
[36] J.H. Boswell, D. Clark, W. Li, and M.M. Attallah, Cracking during thermal post-processing of laser powder bed fabricated CM247LC Ni-superalloy, *Mater. Des.*, 174(2019), art. No. 107793.

[37] B.C. Zhang, X. Lee, J.M. Bai, J.F. Guo, P. Wang, C.N. Sun, M. Nai, G.J. Qi, and J. Wei, Study of selective laser melting (SLM) Inconel 718 part surface improvement by electrochemical polishing, *Mater. Des.*, 116(2017), p. 531.
[38] SLM solutions [2020-12-11]. https://www.slm-solutions.com/industries/aerospace-and-defense/
[39] H.H. Yang, L. Meng, S.C. Luo, and Z.M. Wang, Microstructural evolution and mechanical performances of selective laser melting Inconel 718 from low to high laser power, *J. Alloys Compd.*, 828(2020), art. No. 154473.
[40] M. Amirjan and H. Sakiani, Effect of scanning strategy and speed on the microstructure and mechanical properties of selective laser melted IN718 nickel-based superalloy, *Int. J. Adv. Manuf. Technol.*, 103(2019), No. 5-8, p. 1769.
[41] V.S. Sufiiarov, A.A. Popovich, E.V. Borisov, I.A. Polozov, D.V. Masaylo, and A.V. Orlov, The effect of layer thickness at selective laser melting, *Procedia Eng.*, 174(2017), p. 126.
[42] X.L. Yao, S.K. Moon, B.Y. Lee, and G.J. Bi, Effects of heat treatment on microstructures and tensile properties of IN718/TiC nanocomposite fabricated by selective laser melting, *Int. J. Precis. Eng. Manuf.*, 18(2017), No. 12, p. 1693.
[43] F. Caiazzo, V. Alfieri, and G. Casalino, On the relevance of volumetric energy density in the investigation of Inconel 718 laser powder bed fusion, *Materials*, 13(2020), No. 3, art. No. 538.
[44] X. Li, J.J. Shi, C.H. Wang, G.H. Cao, A.M. Russell, Z.J. Zhou, C.P. Li, and G.F. Chen, Effect of heat treatment on microstructure evolution of Inconel 718 alloy fabricated by selective laser melting, *J. Alloys Compd.*, 764(2018), p. 639.
[45] D.H. Smith, J. Bicknell, L. Jorgensen, B.M. Patterson, N.L. Cordes, I. Tsukrov, and M. Knezevic, Microstructure and mechanical behavior of direct metal laser sintered Inconel alloy 718, *Mater. Charact.*, 113(2016), p. 1.
[46] S.C. Luo, W.P. Huang, H.H. Yang, J.J. Yang, Z.M. Wang, and X.Y. Zeng, Microstructural evolution and corrosion behaviors of Inconel 718 alloy produced by selective laser melting following different heat treatments, *Addit. Manuf.*, 30(2019), art. No. 100875.
[47] B. Izquierdo, S. Plaza, J.A. Sánchez, I. Pombo, and N. Ortega, Numerical prediction of heat affected layer in the EDM of aeronautical alloys, *Appl. Surf. Sci.*, 259(2012), p. 780.
[48] L.L. Parimi, R.G. A, D. Clark, and M.M. Attallah, Microstructural and texture development in direct laser fabricated IN_{718}, *Mater. Charact.*, 89(2014), p. 102.
[49] S. Holland, X.Q. Wang, X.Y. Fang, Y.B. Guo, F. Yan, and L. Li, Grain boundary network evolution in Inconel 718 from selective laser melting to heat treatment, *Mater. Sci. Eng. A*, 725(2018), p. 406.
[50] W.M. Tucho, P. Cuvillier, A. Sjolyst-Kverneland, and V. Hansen, Microstructure and hardness studies of Inconel 718 manufactured by selective laser melting before and after solution heat treatment, *Mater. Sci. Eng. A*, 689(2017), p. 220.
[51] K.N. Amato, S.M. Gaytan, L.E. Murr, E. Martinez, P.W. Shindo, J. Hernandez, S. Collins, and F. Medina, Microstructures and mechanical behavior of Inconel 718 fabricated by selective laser melting, *Acta Mater.*, 60(2012), No. 5, p. 2229.
[52] J. Strößner, M. Terock, and U. Glatzel, Mechanical and microstructural investigation of nickel-based superalloy IN718 manufactured by selective laser melting (SLM), *Adv. Eng. Mater.*, 17(2015), No. 8, p. 1099.
[53] B. Song, S.J. Dong, Q. Liu, H.L. Liao, and C. Coddet, Vacuum heat treatment of iron parts produced by selective laser melting: Microstructure, residual stress and tensile behavior, *Mater. Des.*, 54(2014), p. 727.
[54] M. Ni, S.C. Liu, C. Chen, R.D. Li, X.Y. Zhang, and K.C. Zhou, Effect of heat treatment on the microstructural evolution of a precipitation-hardened superalloy produced by selective laser melting, *Mater. Sci. Eng. A*, 748(2019), p. 275.
[55] W.P. Huang, J.J. Yang, H.H. Yang, G.Y. Jing, Z.M. Wang, and X.Y. Zeng, Heat treatment of Inconel 718 produced by selective laser melting: Microstructure and mechanical properties, *Mater. Sci. Eng. A*, 750(2019), p. 98.
[56] R. Seede, A. Mostafa, V. Brailovski, M. Jahazi, and M. Medraj, Microstructural and microhardness evolution from homogenization and hot isostatic pressing on selective laser melted Inconel 718: Structure, texture, and phases, *J. Manuf. Mater. Process.*, 2(2018), No. 2, art. No. 30.
[57] M. Seifi, A.A. Salem, D.P. Satko, R. Grylls, and J.J. Lewandowski, Effects of post-processing on microstructure and mechanical properties of SLM-processed IN-718, [in] E. Ott, X.B. Liu, J. Andersson, Z.N. Bi, K. Bockenstedt, I. Dempster, J. Groh, K. Heck, P. Jablonski, M. Kaplan, D. Nagahama, and C. Sudbrack, eds., *Proceedings of the 9th International Symposium on Superalloy 718 & Derivatives: Energy, Aerospace, and Industrial Applications*, Pittsburgh, 2018, p. 515.
[58] W. Tillmann, C. Schaak, J. Nellesen, M. Schaper, M.E. Aydinöz, and K.P. Hoyer, Hot isostatic pressing of IN718 components manufactured by selective laser melting, *Addit. Manuf.*, 13(2017), p. 93.
[59] E. Chlebus, K. Gruber, B. Kuźnicka, J. Kurzac, and T. Kurzynowski, Effect of heat treatment on the microstructure and mechanical properties of Inconel 718 processed by selective laser melting, *Mater. Sci. Eng. A*, 639(2015), p. 647.
[60] M.E. Aydinöz, F. Brenne, M. Schaper, C. Schaak, W. Tillmann, J. Nellesen, and T. Niendorf, On the microstructural and mechanical properties of post-treated additively manufactured Inconel 718 superalloy under quasi-static and cyclic loading, *Mater. Sci. Eng. A*, 669(2016), p. 246.
[61] D.Y. Deng, R.L. Peng, H. Brodin, and J. Moverare, Microstructure and mechanical properties of Inconel 718 produced by selective laser melting: Sample orientation dependence and effects of post heat treatments, *Mater. Sci. Eng. A*, 713(2018), p. 294.
[62] T. Trosch, J. Strößner, R. Völkl, and U. Glatzel, Microstructure and mechanical properties of selective laser melted Inconel 718 compared to forging and casting, *Mater. Lett.*, 164(2016), p. 428.
[63] C.H. Pei, W. Zeng, and H. Yuan, A damage evolution model based on micro-structural characteristics for an additive manufactured superalloy under monotonic and cyclic loading conditions, *Int. J. Fatigue*, 131(2020), art. No. 105279.
[64] V.A. Popovich, E.V. Borisov, A.A. Popovich, V.S. Sufiiarov, D.V. Masaylo, and L. Alzina, Impact of heat treatment on mechanical behaviour of Inconel 718 processed with tailored microstructure by selective laser melting, *Mater. Des.*, 131(2017), p. 12.
[65] I.T. Ho, Y.T. Chen, A.C. Yeh, C.P. Chen, and K.K. Jen, Microstructure evolution induced by inoculants during the selective laser melting of IN718, *Addit. Manuf.*, 21(2018), p. 465.
[66] B.C. Zhang, P. Wang, Y. Chew, Y.J. Wen, M.H. Zhang, P. Wang, G.J. Bi, and J. Wei, Mechanical properties and microstructure evolution of selective laser melting Inconel 718 along building direction and sectional dimension, *Mater. Sci. Eng. A*, 794(2020), art. No. 139941.
[67] C.H. Pei, D. Shi, H. Yuan, and H.X. Li, Assessment of mechanical properties and fatigue performance of a selective laser melted nickel-base superalloy Inconel 718, *Mater. Sci. Eng. A*, 759(2019), p. 278.
[68] C. Li, Y.B. Guo, and J.B. Zhao, Interfacial phenomena and characteristics between the deposited material and substrate in selective laser melting Inconel 625, *J. Mater. Process. Technol.*, 243(2017), p. 269.
[69] E. Pavithra and V.S. Senthil Kumar, Microstructural evolution of hydroformed Inconel 625 bellows, *J. Alloys Compd.*,

669(2016), p. 199.
[70] H.B. Zhang, Progress of Inconel 625 alloy abroad, *Spec. Steel Technol.*, 3(2000), p. 69.
[71] C. Li, R. White, X.Y. Fang, M. Weaver, and Y.B. Guo, Microstructure evolution characteristics of Inconel 625 alloy from selective laser melting to heat treatment, *Mater. Sci. Eng. A*, 705(2017), p. 20.
[72] C. Pleass and S. Jothi, Influence of powder characteristics and additive manufacturing process parameters on the microstructure and mechanical behaviour of Inconel 625 fabricated by selective laser melting, *Addit. Manuf.*, 24(2018), p. 419.
[73] I. Koutiri, E. Pessard, P. Peyre, O. Amlou, and T. De Terris, Influence of SLM process parameters on the surface finish, porosity rate and fatigue behavior of as-built Inconel 625 parts, *J. Mater. Process. Technol.*, 255(2018), p. 536.
[74] S. Li, Q.S. Wei, Y.S. Shi, Z.C. Zhu, and D.Q. Zhang, Microstructure characteristics of Inconel 625 superalloy manufactured by selective laser melting, *J. Mater. Sci. Technol.*, 31(2015), No. 9, p. 946.
[75] J. Nguejio, F. Szmytka, S. Hallais, A. Tanguy, S. Nardone, and M. Godino Martinez, Comparison of microstructure features and mechanical properties for additive manufactured and wrought nickel alloys 625, *Mater. Sci. Eng. A*, 764(2019), art. No. 138214.
[76] X.Y. Fang, H.Q. Li, M. Wang, C. Li, and Y.B. Guo, Characterization of texture and grain boundary character distributions of selective laser melted Inconel 625 alloy, *Mater. Charact.*, 143(2018), p. 182.
[77] D.B. Witkin, P. Adams, and T. Albright, Microstructural evolution and mechanical behavior of nickel-based superalloy 625 made by selective laser melting, [in] *Proceedings Volume 9353, Laser 3D Manufacturing II*, San Francisco, 2015.
[78] X.A. Hu, G.L. Zhao, Y. Jiang, X.F. Ma, F.C. Liu, J. Huang, and C.L. Dong, Experimental investigation on the LCF behavior affected by manufacturing defects and creep damage of one selective laser melting nickel-based superalloy at 815 °C, *Acta Metall. Sin. Engl. Lett.*, 33(2020), No. 4, p. 514.
[79] D.B. Witkin, T.V. Albright, and D.N. Patel, Empirical approach to understanding the fatigue behavior of metals made using additive manufacturing, *Metall. Mater. Trans. A*, 47(2016), No. 8, p. 3823.
[80] I. Yadroitsev, L. Thivillon, P. Bertrand, and I. Smurov, Strategy of manufacturing components with designed internal structure by selective laser melting of metallic powder, *Appl. Surf. Sci.*, 254(2007), No. 4, p. 980.
[81] M. Leary, M. Mazur, H. Williams, E. Yang, A. Alghamdi, B. Lozanovski, X.Z. Zhang, D. Shidid, L. Farahbod-Sternahl, G. Witt, I. Kelbassa, P. Choong, M. Qian, and M. Brandt, Inconel 625 lattice structures manufactured by selective laser melting (SLM): Mechanical properties, deformation and failure modes, *Mater. Des.*, 157(2018), p. 179.
[82] K. Mumtaz and N. Hopkinson, Selective laser melting of Inconel 625 using pulse shaping, *Rapid Prototyp. J.*, 16(2010), No. 4, p. 248.
[83] Y.L. Li, L.M. Lei, H.P. Hou, and Y.L. He, Effect of heat processing on microstructures and tensile properties of selective laser melting Hastelloy X alloy, *J. Mater. Eng.*, 47(2019), No. 5, p. 100.
[84] O. Sanchez-Mata, X.L. Wang, J. Muñiz-Lerma, M. Attarian Shandiz, R. Gauvin, and M. Brochu, Fabrication of crack-free nickel-based superalloy considered non-weldable during laser powder bed fusion, *Materials*, 11(2018), No. 8, art. No. 1288.
[85] Germany EOS (Electro Optical Systems) [2021-01-08]. https://www.eos.info/de
[86] D. Tomus, P.A. Rometsch, M. Heilmaier, and X.H. Wu, Effect of minor alloying elements on crack-formation characteristics of Hastelloy-X manufactured by selective laser melting, *Addit. Manuf.*, 16(2017), p. 65.
[87] M.L. Montero-Sistiaga, Z.Z. Liu, L. Bautmans, S. Nardone, G. Ji, J.P. Kruth, J. Van Humbeeck, and K. Vanmeensel, Effect of temperature on the microstructure and tensile properties of micro-crack free Hastelloy X produced by selective laser melting, *Addit. Manuf.*, 31(2020), art. No. 100995.
[88] N.J. Harrison, I. Todd, and K. Mumtaz, Reduction of micro-cracking in nickel superalloys processed by selective laser melting: A fundamental alloy design approach, *Acta Mater.*, 94(2015), p. 59.
[89] D. Tomus, T. Jarvis, X. Wu, J. Mei, P. Rometsch, E. Herny, J.F. Rideau, and S. Vaillant, Controlling the microstructure of Hastelloy-X components manufactured by selective laser melting, *Phys. Procedia*, 41(2013), p. 823.
[90] M.L. Montero-Sistiaga, S. Pourbabak, J. Van Humbeeck, D. Schryvers, and K. Vanmeensel, Microstructure and mechanical properties of Hastelloy X produced by HP-SLM (high power selective laser melting), *Mater. Des.*, 165(2019), art. No. 107598.
[91] F. Calignano and P. Minetola, Influence of process parameters on the porosity, accuracy, roughness, and support structures of Hastelloy X produced by laser powder bed fusion, *Materials*, 12(2019), No. 19, art. No. 3178.
[92] Y.L. Li, H. Qi, H.P. Hou, and L.M. Lei, Effects of hot isostatic pressing on microstructure and mechanical properties of Hastelloy X samples produced by selective laser melting, [in] *Proceedings of the Second International Conference on Mechanics, Materials and Structural Engineering (ICMMSE 2017)*, Beijing, 2017, p. 31.
[93] D. Tomus, Y. Tian, P.A. Rometsch, M. Heilmaier, and X.H. Wu, Influence of post heat treatments on anisotropy of mechanical behaviour and microstructure of Hastelloy-X parts produced by selective laser melting, *Mater. Sci. Eng. A*, 667(2016), p. 42.
[94] D.C. Kong, X.Q. Ni, C.F. Dong, L. Zhang, J.Z. Yao, C. Man, L. Wang, K. Xiao, and X.G. Li, Anisotropic response in mechanical and corrosion properties of Hastelloy X fabricated by selective laser melting, *Constr. Build. Mater.*, 221(2019), p. 720.
[95] Y. Tian, D. Tomus, A.J. Huang, and X.H. Wu, Experimental and statistical analysis on process parameters and surface roughness relationship for selective laser melting of Hastelloy X, *Rapid Prototyp. J.*, 25(2019), No. 7, p. 1309.
[96] Q.Q. Han, Y.C. Gu, S. Soe, F. Lacan, and R. Setchi, Effect of hot cracking on the mechanical properties of Hastelloy X superalloy fabricated by laser powder bed fusion additive manufacturing, *Opt. Laser Technol.*, 124(2020), art. No. 105984.
[97] H.M. Zhang, D.D. Gu, C.L. Ma, M. Guo, J.K. Yang, H. Zhang, H.Y. Chen, C.P. Li, K. Svynarenko, and K. Kosiba, Understanding tensile and creep properties of WC reinforced nickel-based composites fabricated by selective laser melting, *Mater. Sci. Eng. A*, 802(2021), art. No. 140431.
[98] 3D printing industry [2021-01-11]. https://3dprintingindustry.com/news/esa-completes-first-test-fire-of-arianegroup-3d-printed-rocket-engine-149737.